RESEARCH ARTICLE

Onset of solid-state mantle convection and mixing during magma ocean solidification

Maxime Maurice[1], **Nicola Tosi[1,2]**, **Henri Samuel[3,4]**, **Ana-Catalina Plesa[1]**, **Christian Hüttig[1]**, and **Doris Breuer[1]**

[1]Department of Planetary Physics, German Aerospace Center (DLR), Berlin, Germany, [2]Department of Astronomy and Astrophysics, Technische Universität Berlin, Berlin, Germany, [3]Université de Toulouse, UPS-OMP, IRAP, Toulouse, France, [4]IRAP, CNRS, Toulouse, France

Abstract The energy sources involved in the early stages of the formation of terrestrial bodies can induce partial or even complete melting of the mantle, leading to the emergence of magma oceans. The fractional crystallization of a magma ocean can cause the formation of a compositional layering that can play a fundamental role for the subsequent long-term dynamics of the interior and for the evolution of geochemical reservoirs. In order to assess to what extent primordial compositional heterogeneities generated by magma ocean solidification can be preserved, we investigate the solidification of a whole-mantle Martian magma ocean, and in particular the conditions that allow solid-state convection to start mixing the mantle before solidification is completed. To this end, we performed 2-D numerical simulations in a cylindrical geometry. We treat the liquid magma ocean in a parameterized way while we self-consistently solve the conservation equations of thermochemical convection in the growing solid cumulates accounting for pressure-, temperature-, and, where it applies, melt-dependent viscosity. By testing the effects of different cooling rates and convective vigor, we show that for a lifetime of the liquid magma ocean of 1 Myr or longer, the onset of solid-state convection prior to complete mantle crystallization is likely and that a significant part of the compositional heterogeneities generated by fractionation can be erased by efficient mantle mixing. We discuss the consequences of our findings in relation to the formation and evolution of compositional reservoirs on Mars and on the other terrestrial bodies of the solar system.

Plain Language Summary Early in their history, terrestrial planets likely had a molten rocky mantle because of the vast amount of heat released during their formation. They may have been covered by deep oceans of molten rock that are expected to solidify within a few thousand years. The solidification of a magma ocean results in a chemically-stratified mantle with light material at depth and dense, iron-rich material near the top. According to previous models, this gravitationally unstable configuration causes a global overturn, leading to a stably-stratified configuration, which may strongly prevent further creeping flow of the rocky interior, the so-called mantle convection. However, in the case of Mars, its large volcanic provinces along with the evidence for recent volcanism hint at a long-lived dynamic interior, a scenario that is difficult to reconcile with that of a stably stratified mantle. The solidification of a magma ocean can also be accompanied by the growth of a thick atmosphere of water and carbon dioxide, which hinders the cooling of the molten mantle maintaining a high surface temperature through greenhouse effect over a few million years. In this work, we show that, for a slowly solidifying magma ocean, convection can occur in the already solidified mantle and start mixing it while the overlying magma ocean is still solidifying. In contrast to the traditional scenario, no highly unstable configuration is reached at the end of the magma ocean stage. Rather, the planet is left with a partly homogeneous mantle, which can sustain long-term convection in agreement with observations.

1. Introduction

The early processes of planetary accretion and core formation along with the decay of the short-lived radionu-clides ^{26}Al and ^{60}Fe are generally thought to provide sufficient energy to heat the mantle of terrestrial planets up to temperatures that can exceed the liquidus [*Rubie et al.*, 2015], giving birth to large magma ponds [e.g., *Reese and Solomatov*, 2006] or possibly to global magma oceans that may involve part or even the entire mantle [e.g., *Elkins-Tanton*, 2012]. Provided that the planet does not experience subsequent global-scale melting
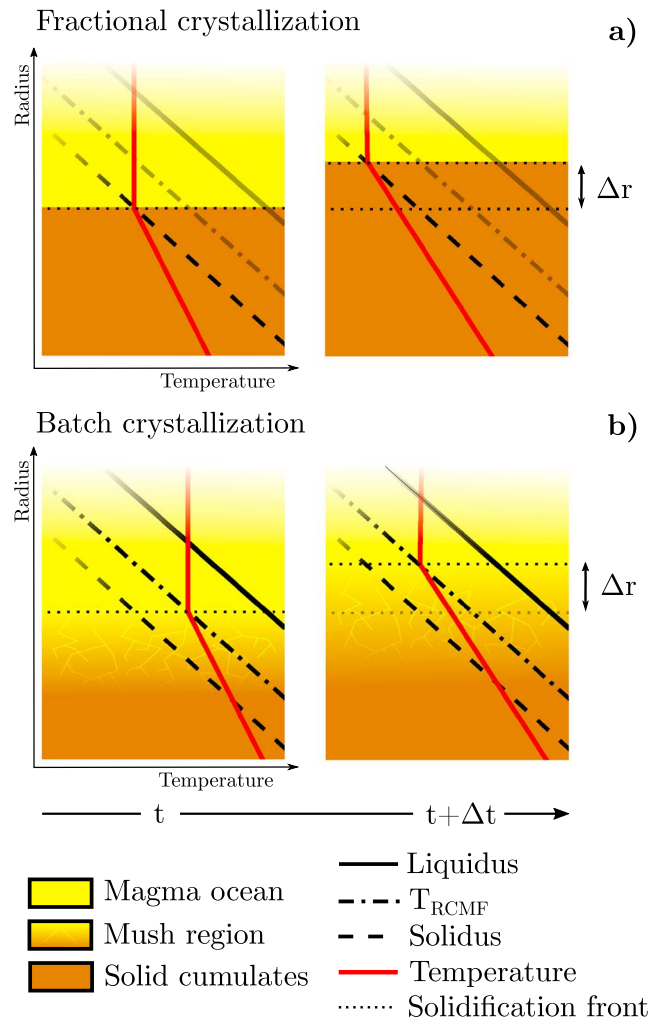
Figure 1. Schematic diagram illustrating the (a) fractional and (b) batch crystallization scenarios. The solidification front lies at the intersection between the magma ocean temperature and the solidus in the fractional case, and the temperature corresponding to the RCMF in the batch case. Over a time step Δt, the fully solid mantle (fractional case) or the mush region (batch case) grows upward by $\Delta r = \Delta t D / t_{MO}$, where D is the thickness of the mantle and t_{MO} the prescribed solidification time of the magma ocean.

events, the crystallization of the last magma ocean represents a crucial step that shapes the initial compositional and thermal structure of the silicate mantle with fundamental consequences for its long-term dynamics and evolution [*Zaranek and Parmentier*, 2004; *Tosi et al.*, 2013; *Plesa et al.*, 2014; *Scheinberg et al.*, 2014].

Because of the very low viscosity of silicate liquids [*Karki and Stixrude*, 2010], a magma ocean is expected to undergo turbulent convection, to efficiently lose heat, and thus to rapidly start solidifying. Since the adiabatic temperature profile in the convecting magma ocean increases with pressure more slowly than the liquidus temperature, solidification proceeds from the core-mantle boundary (CMB) upward (see Figure 1). Bottom-up solidification of the magma ocean is likely to take place in all terrestrial planets of the solar system that are large enough to produce significant adiabatic gradients, including the Earth [e.g., *Fiquet et al.*, 2010; *Andrault et al.*, 2011; *Monteux et al.*, 2016] even though in this case, the possibility exists that crystallization starts from the midmantle [*Stixrude et al.*, 2009].

A commonly assumed scenario for magma ocean solidification consists in its fractionation, with liquid magma being progressively enriched in iron and other incompatible elements with respect to the underlying solid cumulates as cooling and crystallization continue. As a consequence, while the solidification front (i.e., the bottom of the magma ocean and the top of the solid cumulates) moves toward the surface, a compositional stratification progressively forms, with denser and denser cumulates occupying shallower and shallower

mantle layers. Such a configuration is gravitationally unstable and, if mantle convection does not start during magma ocean solidification, it results in an overturn that involves the entire mantle and eventually leads to a stable compositional stratification. Studying this scenario is important because the thermal evolution of a mantle that is initially stably stratified in composition is governed by the physics of double diffusive convection [e.g., *Hansen and Yuen*, 1995] and can be thus entirely different from that of a chemically homogeneous interior in which the dynamics of the mantle is only controlled by thermal convection. In fact, depending on the strength of the compositional gradient, defined by the buoyancy ratio (see section 2.2), a variety of convective planforms can be obtained. Convection can take place in separate layers, or in a well-mixed upper layer overlying a stably stratified lower mantle, or can be shaped by large thermochemical piles [*Zaranek and Parmentier*, 2004; *Tosi et al.*, 2013] that may bear resemblance to the two large low-shear-velocity provinces that characterize the long-wavelength thermochemical structure of the Earth's deep mantle [e.g., *Garnero et al.*, 2016]. Moreover, characterizing the thermal and compositional state of the mantle after the solidification of a magma ocean provides important conditions for the emergence of its subsequent tectonic regime [*Foley et al.*, 2014; *O'Neill et al.*, 2016].

The fractional crystallization of a magma ocean, possibly followed by a whole-mantle overturn, is a mechanism that has been proposed to explain various features of the early evolution of Mercury [*Brown and Elkins-Tanton*, 2009], Mars [*Elkins-Tanton et al.*, 2005a; *Scheinberg et al.*, 2014], the Moon [*Zhong et al.*, 2000; *de Vries et al.*, 2010; *Zhang et al.*, 2013], and the Earth [*Foley et al.*, 2014; *Boukaré et al.*, 2015]. In the context of Mars, in particular, the fractional crystallization of a global magma ocean, originally proposed by *Elkins-Tanton et al.* [2003], has been invoked to explain the formation of an ancient crust with composition consistent with surface and meteoritic data [*Elkins-Tanton et al.*, 2005b]; to explain radioactive isotopes systematics of the SNC meteorites in terms of distinct mantle reservoirs that may have been sustained by the stable structure resulting from a global overturn [*Debaille et al.*, 2007, 2009] (see section 4.2.2); and to account for an early episode of dynamo activity induced by the overturn of mantle cumulates [*Elkins-Tanton et al.*, 2005a]. Despite these successes, the fractional crystallization scenario also poses problems for the long-term evolution of the mantle. In particular, the compositional gradient inferred from petrological modeling [*Elkins-Tanton et al.*, 2005b] is sufficiently large to completely suppress any form of thermal or thermochemical mantle convection after the cumulate overturn [*Tosi et al.*, 2013; *Plesa et al.*, 2014]. This, in turn, strongly limits in time partial melt generation, which, under these conditions, can only occur over the first few hundred million years of evolution [*Plesa et al.*, 2014]. This picture is indeed difficult to reconcile with Mars's large volcanic provinces and long-lasting volcanic activity, which are likely the products of billions of years of vigorous mantle convection [e.g., *Li and Kiefer*, 2007; *O'Neill et al.*, 2007; *Grott and Breuer*, 2010; *Sekhar and King*, 2014].

One possibility that may help in resolving the above issues is that Mars's magma ocean underwent a combination of batch (i.e., equilibrium) and fractional crystallization, similar to what has been proposed by *Solomatov* [2000] for the batch crystallization of the Earth's lower mantle followed by the fractional crystallization of the upper mantle. In this case, the compositional gradient established at the end of solidification would not be as strong as in the purely fractional case. This would facilitate the onset of post-overturn mantle convection [*Tosi et al.*, 2013] and yet allow for the long-term preservation of primordial compositional heterogeneities as suggested by the isotopic signatures of the SNC meteorites [e.g., *Foley et al.*, 2005].

Fractional crystallization of the entire magma ocean relies on the hypothesis that the timescale of mantle solidification is shorter than the timescale for the onset of the convective cumulates overturn. Highly efficient heat loss due to turbulent convection in the magma ocean can indeed ensure that the entire mantle crystallizes very rapidly with a timescale of the order of 10^3 years [*Monteux et al.*, 2016], unless a thick atmosphere generated by volatile degassing builds up [e.g., *Abe and Matsui*, 1985; *Zahnle et al.*, 1988; *Abe*, 1993]. In this case, the time over which the solidification front reaches the surface becomes of the order of $10^5 - 10^6$ years [*Zahnle et al.*, 2007; *Lebrun et al.*, 2013]. The magma ocean solidification time is defined here as the time until a liquid-like, turbulently convecting layer can be maintained at the surface of the planet, allowing for efficient heat extraction. Over the above timescales, newly formed solid cumulates with high, near-solidus temperatures and hence low viscosity, possibly further reduced by the presence of residual melt, can begin overturning before the solidification front has reached the surface. Solid-state convection can start mixing compositional heterogeneities while solidification is still taking place, thus effectively reducing the final compositional gradient due to fractional crystallization.

By employing numerical convection simulations in a 2-D quarter of cylinder domain with a moving upper boundary that mimics the solidification front, we investigate the conditions for the initiation of solid-state thermochemical convection during magma ocean solidification. We treat the two end-member scenarios of batch and fractional crystallization and demonstrate that in both cases, for the cooling rates that can be expected in the presence of an insulating atmosphere, thermal and compositional mixing via solid-state convection can start soon after the formation of the first solid mantle cumulates.

The paper is organized as follows. In section 2 we present in detail our model, including the treatment of fractional and batch crystallization of the magma ocean (2.1), the equations governing the dynamics of the solidifying mantle (2.2), the set of parameters tested (2.3), the numerical setup (2.4), and the description of mantle mixing characterization (2.5). Section 3 contains the results on the onset of convection (3.1) and on the characteristics of mantle mixing during magma ocean solidification (3.2). The results are discussed in section 4 in the context of the early evolution of the mantle of Mars (4.1 – 4.3) and of the other terrestrial bodies (4.4). Conclusions are presented in section 5.

2. Model

2.1. Magma Ocean Solidification

As mentioned above, because of the steeper slope of the magma ocean adiabat with respect to the melting curves, mantle solidification starts at the CMB and proceeds upward until the solidification front reaches the surface. We consider a Mars-like body whose mantle is initially completely molten except for a thin layer atop the CMB that is assumed to have already solidified (see section 2.4). The magma ocean temperature follows the temperature reached at the solidification front, which depends on the chosen crystallization scenario (see sections 2.1.1 and 2.1.2 and Figure 1). For simplicity, and since we are not aiming at reproducing the physics of the liquid magma ocean itself, we assume that the thermal evolution of the magma ocean results in a rise of the solidification front linear in time, an assumption that we discuss in section 4.3. The time needed to achieve complete solidification of the magma ocean (t_{MO}) is one of the investigated parameters. For the solidus and liquidus curves, we use parameterizations proposed by *Herzberg et al.* [2000] and *Zhang and Herzberg* [1994], respectively, which are based on melting experiments conducted on fertile KLB-1 peridotite. According to these two studies, solidus and liquidus temperatures (respectively, T_{sol} and T_{liq}) can be expressed as a function of hydrostatic pressure P as follows:

$$T_{sol} = 1400 + 149.5P - 9.64P^2 + 0.313P^3 - 0.0039P^4, \tag{1}$$

$$T_{liq} = 1977 + 64.1P - 3.92P^2 + 0.141P^3 - 0.0015P^4, \tag{2}$$

where T_{sol} and T_{liq} are expressed in K and P in GPa.

In order to assess the consequences of magma ocean solidification for the dynamics of the solid mantle, we treat the two end-member scenarios of fractional and batch crystallization [*Solomatov*, 2007], which are described below.

2.1.1. Fractional Crystallization

In the fractional crystallization scenario, we assume that residual melt cannot remain within the solid matrix and is extracted into the overlying liquid, leaving beneath a differentiated solid mantle. In this case, the temperature of the solidification front simply coincides with the solidus (Figure 1a). Upon solidification, iron is preferentially partitioned into the liquid phase [e.g., *Elkins-Tanton et al.*, 2005b], which causes the enrichment of the magma ocean and, in turn, of the latest (i.e., shallowest) solidified layers. As a consequence, an unstable compositional profile forms, with progressively denser cumulates that occupy shallower and shallower mantle layers.

This scenario is qualitatively similar to the one considered in previous studies [e.g., *Elkins-Tanton et al.*, 2005b; *Tosi et al.*, 2013; *Plesa et al.*, 2014; *Scheinberg et al.*, 2014]. The fundamental difference here is that instead of assuming the entire unstable compositional profile to be built before any solid-like mantle overturn can take place, we model its formation allowing for the possibility that solid-state convection sets in before the solidification front has reached the surface (see section 2.2).

It must be also noted that, because of chemical partitioning, the actual solidus of the crystallizing cumulates should evolve as the solidification proceeds. At the beginning, when the most mafic materials crystallize,

it would correspond to the liquidus of the bulk mantle, while at the end, when the most felsic materials crystallize, it would correspond to its solidus. However, for simplicity, we only use here the solidus of the bulk mantle, which, in turn, translates into a lower temperature, and hence a higher viscosity at the solidification front for the deepest cumulates (see section 2.2).

2.1.2. Batch Crystallization

As an alternative to the fractional crystallization scenario, we consider a simple model of batch crystallization where the melt remains entirely embedded in the matrix until solidification is completed, thus leading to a homogeneous mantle composition. This situation could be encountered if, for example, the mantle solidified rapidly, over a time shorter than the characteristic timescale for melt percolation and crystal segregation, or if the melt was neutrally buoyant.

Between the liquidus and solidus, the volumetric melt fraction ϕ decreases linearly with temperature from 1 to 0:

$$\phi = \frac{T - T_{sol}}{T_{liq} - T_{sol}}. \tag{3}$$

Experiments show that the rheology of two-phase crystal-melt mixtures presents a sharp transition between liquid-like and solid-like behavior around a certain rheologically critical melt fraction (RCMF) [e.g., *Costa et al.*, 2009]. The RCMF identifies the critical value of ϕ below, in which newly formed crystals build an interconnected network that effectively deforms via solid-state creep, which can be treated by solving the equations of mantle convection (section 2.2). In the batch crystallization case, the temperature of the solidification front is no longer the solidus as in the fractional case, but the temperature T_{RCMF} corresponding to the RCMF (Figure 1b). The partially molten region where the temperature lies between T_{sol} and T_{RCMF}, the so-called mush domain [*Solomatov*, 2007], is thus treated as part of the solid mantle with a viscosity, which, besides being dependent on temperature and pressure, also depends on the melt fraction (see section 2.2 and equations (10) and (11)).

Note that in the both crystallization scenarios, the end of magma ocean solidification corresponds to the time when the solidification front reaches the surface, which means the time when the surface temperature reaches the solidus in the fractional crystallization case, or the RCMF temperature in the batch crystallization case.

2.2. Mantle Convection

To simulate the dynamics of the solid cumulates upon magma ocean solidification, we solve the nondimensional conservation equations of mass, momentum, thermal energy, and composition under the Boussinesq approximation [e.g., *Schubert et al.*, 2001]. These read, respectively,

$$\vec{\nabla} \cdot \vec{u} = 0, \tag{4}$$

$$\vec{\nabla} \cdot [\eta(\vec{\nabla}\vec{u} + (\vec{\nabla}\vec{u})^T)] - \vec{\nabla}p + Ra_{ref}(T - BC)\vec{e}_r = \vec{0}, \tag{5}$$

$$\frac{\partial T}{\partial t} + \vec{u} \cdot \vec{\nabla}T - \nabla^2 T = 0, \tag{6}$$

$$\frac{\partial C}{\partial t} + \vec{u} \cdot \vec{\nabla}C = 0, \tag{7}$$

where $\vec{u}$ is the velocity, η the dynamic viscosity, p the dynamic pressure, Ra_{ref} the reference thermal Rayleigh number, T the temperature, B the buoyancy ratio, C the compositional density field, and $\vec{e}_r$ the unit vector in radial direction. The Rayleigh number and buoyancy ratio are defined as follows:

$$Ra_{ref} = \frac{\alpha \rho g \Delta T D^3}{\kappa \eta_{ref}}, \tag{8}$$

$$B = \frac{\Delta \rho_C}{\rho \alpha \Delta T}, \tag{9}$$

where α is the coefficient of thermal expansion, ρ the reference mantle density, g the gravitational acceleration, ΔT the temperature scale, κ the thermal diffusivity, η_{ref} the reference viscosity, and $\Delta \rho_C$ the maximum density difference due to composition (see Table 1 for the numerical values). The Rayleigh number describes the ratio of buoyancy forces due to thermal expansion and contraction to the stabilizing effects of heat and momentum diffusion, while the buoyancy ratio measures the importance of density contrasts associated with

Table 1. Variables and Parameters Used in the Simulations Accompanied by Their Scaling, Definition, and/or Numerical Value (Either Dimensional for Material Parameters and Physical Quantities or Nondimensional in the Case of the Various Nondimensional Groups)

Variable/Parameter	Symbol	Value	Scaling/Definition
Time	t	–	D^2/κ
Radial unit vector	$\vec{e}_r$	–	D
Velocity vector	$\vec{u}$	–	κ/D
Dynamic pressure	p	–	$\eta_{ref}/(\kappa D)$
Temperature	T	–	ΔT
Composition	C	–	$\Delta\rho_C$
Viscosity	η	–	η_{ref}
Planet radius	R_p	3400 km	D
Core radius	R_c	1700 km	D
Mantle thickness	D	1700 km	–
Gravitational acceleration	g	3.7 m/s^2	–
Initial thickness of solid domain	D_0	170 km	D
Magma ocean cooling time	t_{MO}	0.1, 1, 10 Myr	D^2/κ
Reference viscosity at (T_{ref}, z_{ref})	η_{ref}	4.4×10^{17}, 4.4×10^{18}, 4.4×10^{19} Pa s	–
Reference temperature	T_{ref}	2503 K	ΔT
Reference depth	z_{ref}	1700 km	D
Activation energy	E	3.35×10^5 J/mol	$R\Delta T$
Activation volume	V	4×10^{-6} m^3/mol	$R\Delta T/(\rho g D)$
Melt viscosity factor	β	21	–
RCMF	ϕ_{RCMF}	0.3	–
Gas constant	R	8.313 J/(kg mol)	–
Mantle heat capacity	c_p	1200 J/(kg K)	–
Mantle thermal diffusivity	κ	10^{-6} 1/m^2	–
Mantle thermal expansivity	α	3×10^{-5} K^{-1}	–
Mantle reference density	ρ	3500 kg/m^3	–
Core heat capacity	$c_{p,c}$	840 J/(kg K)	–
Core density	ρ_c	7200 kg/m^3	–
Temperature scale	ΔT	2283 K	–
Surface temperature	T_s	220 K	ΔT
Compositional density scale	$\Delta\rho_c$	47.8, 239, 430 kg/m^3	–
Reference Rayleigh number	Ra_{ref}	10^8, 10^9, 10^{10} Pa s	$\rho g\alpha\Delta T D^3/(\eta_{ref}\kappa)$
Buoyancy ratio	B	0.2, 1, 1.8	$\Delta\rho_C/(\rho\alpha\Delta T)$

variations in composition with respect to density contrasts due to variations in temperature. Note that in our simulations, both the initial temperature and the initial compositional gradient act in favor of the onset of convection rather than compete against each other. It is only after the first overturn has taken place that compositional buoyancy acts against thermal convection. Also, note that in equation (6) we neglected internal heating. On the one hand, in the case of fractional crystallization, heat-producing elements, being highly incompatible, would be strongly enriched initially in the liquid phase and, toward the end of solidification, in the shallow solid cumulates [see *Plesa et al.*, 2014; *Scheinberg et al.*, 2014, and references therein]. As a consequence, the bulk of the solid mantle is likely depleted in heat sources during crystallization. On the other hand, in the case of batch crystallization, tests conducted with and without internal heating did not evidence significant differences in the onset time of convection, which is largely controlled by the very low viscosity caused by the high temperature and by the presence of melt (section 3.1).

In the fractional crystallization case, we use the nondimensional field C to model the evolving composition of the solid cumulates assuming for simplicity that C grows linearly from the CMB (where $C = 0$), to the surface

(where $C = 1$) [*Tosi et al.*, 2013]. The buoyancy ratio B is used as model parameter to control the strength of the compositional gradient (section 2.3).

All material parameters (see Table 1 for the numerical values) are assumed to be constant with the exception of the density, which, according to the Boussinesq approximation, varies only when it appears in the buoyancy terms through the Rayleigh number and buoyancy ratio (equation (5)) and of the viscosity, which is assumed to depend on temperature and depth according to the Arrhenius law for diffusion creep whose nondimensional form reads as follows [*Roberts and Zhong*, 2006]:

$$\eta(T, z) = \exp\left(\frac{E + zV}{T + T_s} - \frac{E + z_{\text{ref}}V}{T_{\text{ref}} + T_s}\right), \tag{10}$$

where E and V are activation energy and volume characteristic of diffusion creep of olivine [*Hirth and Kohlstedt*, 2003], z is the depth, T_s is the surface temperature, and z_{ref} and T_{ref} are reference values of depth and temperature, respectively. All variables and parameters in equation (10) are nondimensional.

In the case of batch crystallization, for temperatures between the T_{RCMF} and T_{sol}, we take into account the supplementary effect of the presence of melt on the viscosity through an additional exponential term [e.g., *Hirth and Kohlstedt*, 2003; *Scott and Kohlstedt*, 2006]:

$$\eta_{\text{batch}} = \eta(T, z)\exp(-\beta\phi), \tag{11}$$

where β is a parameter derived from laboratory experiments that in our simulations is set to 21 [*Scott and Kohlstedt*, 2006]. It should be noted that although the actual value of the RCMF can strongly vary according to the type and shape of crystals [*Saar et al.*, 2001], here we make the rather standard choice of setting $\phi_{\text{RCMF}} = 0.3$ [e.g., *Scott and Kohlstedt*, 2006], which does not lead to extremely low viscosities that would be difficult to deal with numerically.

The dimensional viscosity field is obtained by scaling the nondimensional viscosity (10) or (11) with the reference viscosity η_{ref}, which is the viscosity at temperature T_{ref} and depth z_{ref}, calculated using activation parameters for diffusion creep of olivine according to *Hirth and Kohlstedt* [2003] (see section 2.3).

In both crystallization scenarios, the temperature of the solid cumulates cannot exceed its initial value, i.e., the solidus for the fractional crystallization scenario and the RCMF temperature for the batch crystallization scenario. The melt that would be generated by hot upwelling cumulates whose temperature rises above these thresholds is assumed to be extracted instantaneously into the overlying liquid magma ocean. Also, note that latent heat effects are not explicitly included but their consequences are discussed in section 4.3.

2.3. Parameters

We investigate the onset of solid-state convection for the two crystallization scenarios by varying the following parameters: the reference Rayleigh number Ra_{ref}, the magma ocean solidification time t_{MO}, and, in case of fractional crystallization, the buoyancy ratio B. In the case of batch crystallization, we assume a homogeneous mantle with no compositional heterogeneities, i.e., with $B = 0$ (see section 2.1.2). The reference Rayleigh number Ra_{ref} corresponding to the reference viscosity η_{ref} is defined at the depth of the CMB ($z_{\text{ref}} = 1$), and at the temperature of 2503 K, i.e., the temperature of the RCMF at the CMB for which $T_{\text{ref}} = 1$. We varied Ra_{ref} between 10^8, 10^9, and 10^{10} for the fractional crystallization and set it to 10^7 for the batch crystallization cases (see section 3.1). These values correspond to reference viscosities of $\eta_{\text{ref}} = 4.4 \times 10^{20}$, 4.4×10^{19}, and 4.4×10^{18} Pa s, respectively, in the fractional crystallization case, and 4.4×10^{21} Pa s in the batch crystallization cases. At the more conventional reference pressure and temperature of 3 GPa and 1600 K often employed in studies of mantle convection and thermal evolution [e.g., *Tosi et al.*, 2013; *Plesa et al.*, 2014], the above reference viscosities would be 2.4×10^{22}, 2.4×10^{21}, and 2.4×10^{20} Pa s, respectively, in the fractional crystallization case and 2.4×10^{23} Pa s in the batch crystallization cases, yielding Rayleigh numbers of 1.23×10^5, 1.23×10^6, and 1.23×10^7, respectively, for the fractional crystallization cases, and 1.23×10^4 for the batch crystallization cases. Note that η_{ref} can be formally calculated by changing the preexponential term of the olivine flow law for diffusion creep using different values of the grain size and/or of the water content [*Hirth and Kohlstedt*, 2003]. The values that we used have been obtained by setting the grain size to 1 cm and varying the water content between 1, 10, and 100 ppm. Furthermore, in the case of batch crystallization, the presence of interstitial melt further decreases the effective viscosity (see equation (11) and section 3.1).

The magma ocean solidification time (t_{MO}), defined as the time necessary for the solidification front to propagate from the CMB to the surface, is varied between 0.1, 1, and 10 Myr. These values are representative of relatively long-lived magma oceans whose crystallization is slowed down by the blanketing effect of a growing H_2O-CO_2 atmosphere generated upon degassing of greenhouse volatiles [*Abe*, 1993; *Hamano et al.*, 2013; *Lebrun et al.*, 2013].

In the case of fractional crystallization, we test three different values of the buoyancy ratio: B = 0.2, 1, and 1.8, corresponding to maximum compositional density contrasts $\Delta \rho_C$ between the surface and the CMB of 47.8, 239, and 430 kg/m^3, respectively.

2.4. Numerical Setup

To solve equations (4)–(7), we used the finite volume code GAIA [*Hüttig et al.*, 2013; *Hüttig and Stemmer*, 2013] in a two-dimensional quarter of a cylindrical domain with a moving upper boundary. A thin initial solid layer is prescribed so that the actual solution domain is present from the beginning. In all simulations, we used a shell with an initial thickness D_0 = 170 km that mimics the first solid cumulate layer above the CMB. The subsequent bottom-up crystallization of the magma ocean is modeled by progressively increasing the size of the solid domain at a predefined rate according to the parameter t_{MO} and considering a growth linear in time (section 2.3) until the solidification front reaches the planetary surface (whose radius is assumed to be twice as large as the core radius as appropriate for a Mars-like body). The upper and lower boundaries of the growing partial cylinder shell have free-slip conditions and a prescribed temperature. The temperature of the upper boundary evolves according to the position of the solidification front, following either the profile of T_{sol} or T_{RCMF} depending on the crystallization scenario (section 2.1). The CMB temperature T_{CMB} corresponds initially to the CMB temperature of the solidus (in fractional crystallization cases) or of the RCMF (in batch crystallization cases) and evolves following a standard energy balance assuming the core to be a homogeneous medium with given density and heat capacity [e.g., *Stevenson et al.*, 1983]:

$$c_{p,c} \rho_c V_c \frac{dT_{CMB}}{dt} = -q_c A_c, \qquad (12)$$

where $c_{p,c}$ is the core heat capacity, ρ_c the core density, V_c the core volume, q_c the heat flux at the CMB, i.e., $q_c = c_p \rho \kappa (\partial T / \partial r)_{CMB}$, the temperature gradient being computed between the lowest shell of the resolved domain and the T_{CMB}, and A_c the outer area of the core.

The initial temperature distribution follows the profiles of T_{sol} in the fractional case, or of T_{RCMF} in the batch case, beneath the rising solidification front. Note that for short lifetimes of the magma ocean and relatively small reference Rayleigh numbers, the solidification front will likely reach the surface before the onset of solid-state convection. In that case, the initial temperature distribution is the entire solidus (for fractional crystallization) or the entire profile of T_{RCMF} (for batch crystallization). Also, note that the surface temperature is set to its present-day value as soon as the solidification front reaches the surface. After the cessation of the liquid magma ocean phase, in fact, a very high surface temperature can be hardly sustained. Indeed, at least for the Earth, *Valley et al.* [2005] show that there is evidence that a cold surface may have been present as early as 4.4 Ga. Because of the strong temperature dependence of the viscosity, this causes the rapid formation of a stagnant lid since no plastic yielding is taken into account. To initiate convection, a random perturbation with an amplitude of 10^{-3} is added to the initial temperature profile.

In the fractional crystallization case, an unstable compositional profile that grows linearly from the CMB upward [*Tosi et al.*, 2013] is progressively built up as the magma ocean solidifies. The transport equation (7) governing the advection of the composition field is solved using the particle-in-cell method as implemented in GAIA [*Plesa et al.*, 2012].

We selected the resolution of our finite volume mesh according to the reference Rayleigh number. We used 100 radial shells for $Ra_{ref} = 10^8$, 150 shells for $Ra_{ref} = 10^9$, and 200 shells for $Ra_{ref} = 10^{10}$, with each shell containing, respectively, 237, 355, and 473 grid cells in the lateral direction. In order to reliably capture the onset of convection, a high temporal resolution is also essential [e.g., *Korenaga and Jordan*, 2003]. We chose the time step Δt according to the Courant criterion, i.e., $\Delta t = Co \, \delta_{min}/|u|_{max}$, where δ_{min} is the minimum spatial resolution in the radial or lateral direction, $|u|_{max}$ is the maximum velocity locally attained in the domain, and Co is the Courant number that we set to 0.5 in all simulations. In addition, we limited the actual value of Δt by defining a maximum nondimensional time step $\Delta t_{max} = 10^{-8}$ (corresponding to ~900 years) that was used whenever the Courant criterion would result in a larger time step.

For a representative run that leads to an early onset of convection with $Ra_{ref} = 10^9$, $t_{MO} = 10$ Myr, and $B = 1$, we carried out resolution tests by varying both the spatial and temporal resolution of the simulation. Tests conducted using 100 to 250 radial shells and setting Δt_{max} between 10^{-7} and 10^{-9} did not evidence significant differences in terms either of the onset time of solid-state convection or of its characteristic planform. Specifically, the time for the onset of convection varies by up to 0.04 Myr upon varying the temporal resolution and 0.06 Myr upon varying the spatial resolution within the above ranges.

2.5. Characterization of Mantle Mixing

In the fractional crystallization cases, where a compositional field is advected, we monitor the mixing of the mantle due to convection. Once convection sets in, due to the action of the local velocity field and its corresponding velocity gradient tensor, $\mathbf{J} = \vec{\nabla}\vec{u}$, each mantle parcel will stretch and shrink along preferential directions. In the frame of the Boussinesq approximation assumed here (section 2.2), these two directions are perpendicular. Following *Farnetani and Samuel* [2003], in a two-dimensional domain, the maximum strain along the stretching and shrinking directions are derived from the Lagrangian time integration of the following equation for the entries of a 2×2 linear operator matrix:

$$\frac{D\mathbf{M}}{Dt} = \mathbf{JM},$$ (13)

subject to the initial condition of $\mathbf{M}(t = 0)$ being the identity matrix. Along a flow streamline, $\mathbf{M}$ relates the vectors connecting two small, initially close, fluid parcels from $\vec{r}_0 = \vec{r}(t = 0)$ to $\vec{r}(t) = \mathbf{M}\vec{r}_0$. The maximum amount of stretching and shrinking at a given time and location correspond to σ^+ and σ^-, the maximum and minimum eigenvalues of $\mathbf{M}$, respectively. The incompressibility constraint (equation (4)) implies that $\sigma^- = 1/\sigma^+$.

We characterize the efficiency of mixing for each model by monitoring σ^-, the maximum shrinking factor. This quantity is initially equal to unity. For a velocity field-generating deformation, σ^- decreases toward a minimum asymptotic value of 0. Low values of σ^- indicate stronger shortening of mantle parcels with larger aspect ratio, favoring mixing and homogenization with the surroundings via chemical diffusion [*Olson et al.*, 1984; *Gurnis*, 1986; *Ottino*, 1989]. Equivalently, this quantity expresses the amount by which the initial size of a mantle parcel has been reduced as a result of the deformation along its trajectory [*Samuel et al.*, 2011; *Samuel and King*, 2014]. In other words, for a mantle parcel of given initial size δ_0, its dimension in the direction of maximum shrinking at time t is just $\delta = \delta_0\sigma^-$, implying that the smaller the σ^-, the more efficient is mixing. Maximum shrinking factors are tracked along as many trajectories as grid cells, whose initial locations are spread over the computational domain according to a random homogeneous distribution. Equation (13) is then integrated forward in time using a second-order predictor-corrector Runge-Kutta method with bilinear interpolation of velocity components located at the four nearest grid points.

With respect to studies in which convective mixing is discussed on the basis of the distribution of tracers [e.g., *O'Neill et al.*, 2013; *Tosi et al.*, 2013], the calculation of the shrinking factor has the advantage of allowing us to characterize with a single number the mixing properties of each of the analyzed cases (see section 3.2).

3. Results

3.1. Onset of Solid-State Convection

The onset of convection during the magma ocean solidification results from a competition between the timescale of the first convective overturn and the timescale of solidification (t_{MO}), the former being influenced by the reference Rayleigh number Ra_{ref} and, in the case of fractional crystallization, also by the buoyancy ratio B. From now on, we will speak of "early" onset of convection if this occurs before the end of the solidification of the magma ocean and of "late" onset if convection begins only afterward, resulting in a global-scale overturn occurring underneath a stagnant lid.

Figure 2 shows the evolution of a representative case characterized by an early onset of convection. In this example, we considered a fractional crystallization model with the following parameters: $Ra_{ref} = 10^{10}$, $B = 1.8$ and $t_{MO} = 1$ Myr. Figure 2a shows the initial conditions. The semitransparent layer denotes the parameterized magma ocean region (i.e., the region where the conservation equations are not solved); the opaque layer, which is colored according to the composition field and grows radially outward with time, represents the solid cumulates with an initial temperature (red line) set at the solidus (black dashed line), and an initial composition set to a linear unstable gradient (blue line). After 0.7 Myr the first overturn has already taken place
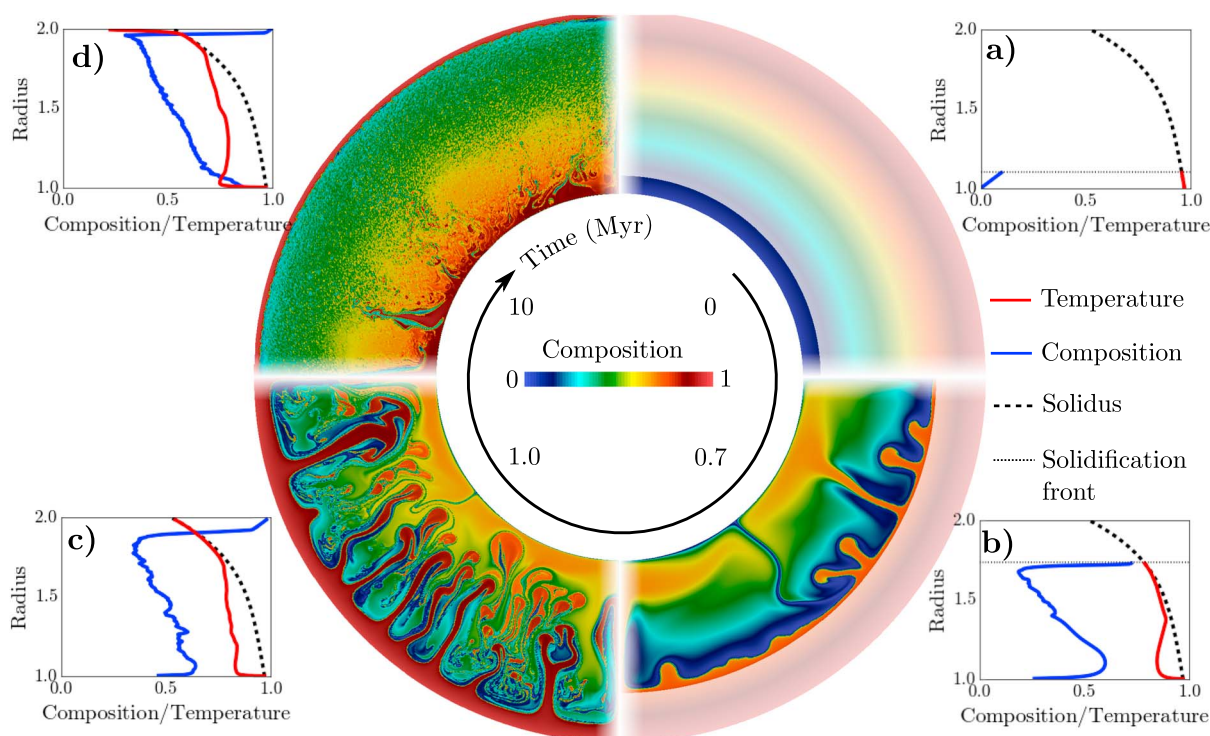
Figure 2. Evolution of the composition field for a fractional crystallization model with $Ra_{ref} = 10^{10}$, $B = 1.8$, and $t_{MO} = 1$ Myr. The four panels show snapshots and corresponding laterally averaged profiles of temperature (red line) and composition (blue line) at the (a) beginning of the simulation, and (b) after 0.7 Myr, (c) 1 Myr, and (d) 10 Myr. The black dashed and dotted lines denote the solidus temperature and the position of the solidification front, respectively.

(Figure 2b). Compositionally dense material accumulates near the CMB, while lighter material is driven below the solidification front by hot upwellings. At 1 Myr, the solidification is completed. By this time, the initial compositional gradient is significantly reduced as shown by the composition profile in Figure 2c, indicating a relatively well-mixed interior. For the subsequent evolution, the surface temperature is set to its present-day value, which quickly creates a highly viscous stagnant lid in absence of yielding (which is not included in the model), slowly delaminated by dripping downwellings caused by the underlying convection. At 10 Myr most of the densest cumulates that formed near the surface have either sunken at the CMB or have been mixed by mantle convection with the consequence that the effective buoyancy ratio of the convecting part of the mantle is much lower than in the case of a whole-mantle overturn (Figure 2d).

In order to investigate how the onset of convection is influenced by the various model parameters, we followed the evolution of the Nusselt number calculated at the bottom of the domain (Nu_{bot}). Defined as the ratio of the total heat flux (convective and conductive) to the conductive heat flux only, the Nusselt number can be effectively used to track the onset of finite-amplitude convection. As long as heat is transported by conduction, Nu_{bot} will be equal to one, while it will become higher as soon as convection sets in. Figure 3 shows time series of Nu_{bot} for all simulations over a time interval of 11 Myr.

An early onset of mantle convection is only possible if the solidification time of the magma ocean is sufficiently long in comparison with the convective overturn timescale. Therefore, the fast solidifying cases (small values of t_{MO}) generally result in a late onset of convection. This is the case, in fact, for all the cases with $t_{MO} = 0.1$ Myr, regardless of Ra_{ref} or B. With $t_{MO} = 1$ Myr, however, in the fractional crystallization cases, early onset of convection occurs for $Ra_{ref} \geq 10^{10}$ and, with $t_{MO} = 10$ Myr, for $Ra_{ref} \geq 10^9$. If increasing the buoyancy ratio slightly shifts the time of onset of convection toward earlier values, it does not have a first-order influence as the value of Ra_{ref} does. This reflects the fact that our uncertainty in the density contrast spans not more that 1 order of magnitude, whereas the uncertainty in the viscosity covers (in this study) 3 orders of magnitude.

The convective phase always begins with an intense overturn involving the thermal and compositional density contrasts available at the time of the onset. This first overturn is then followed by a less intense phase during which thermal convection acts against the stabilizing effect of the overturned cumulates. This behavior
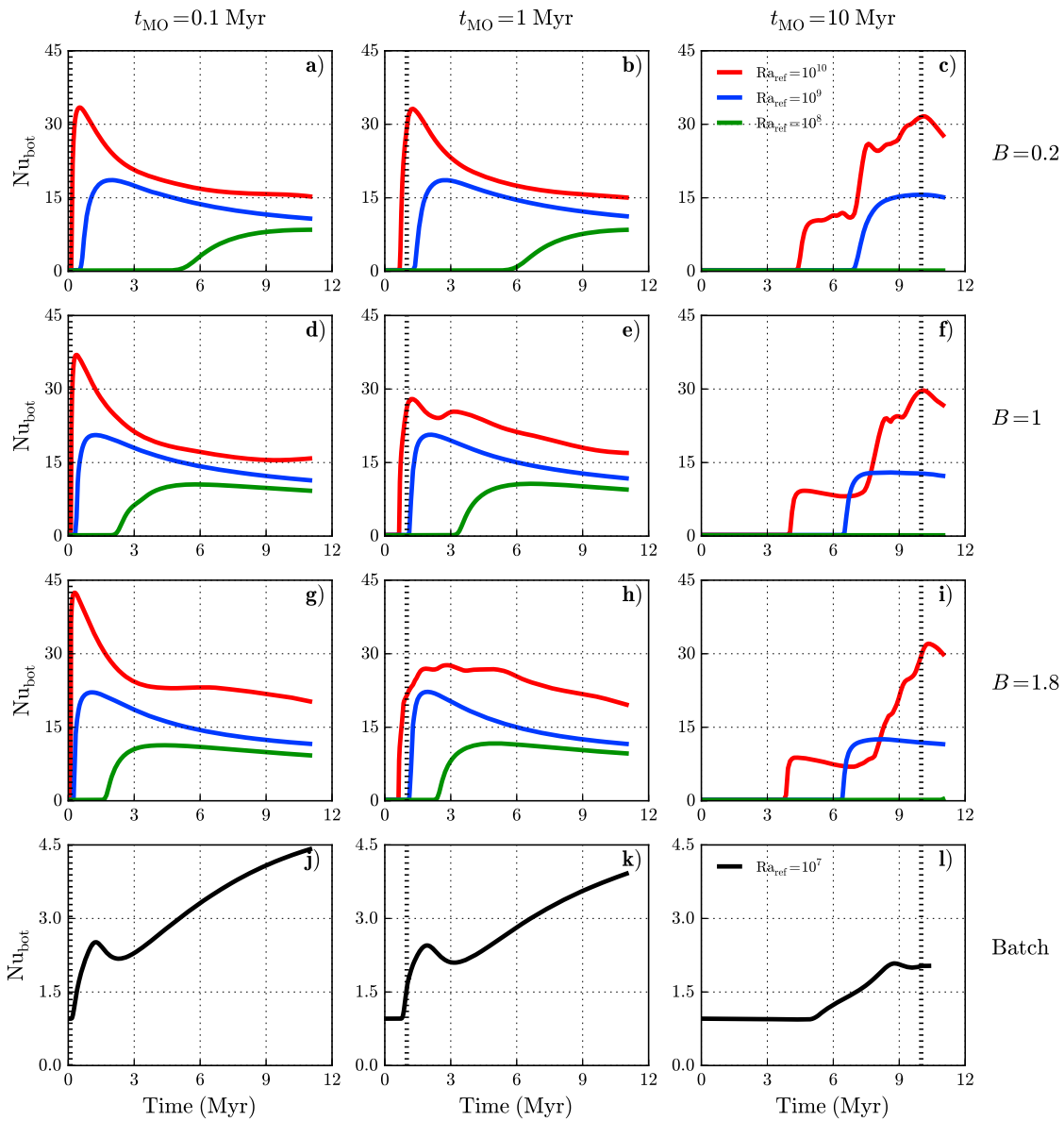
Figure 3. Time series of the bottom Nusselt number for all combinations of parameters. (a–i) Fractional models ($B > 0$) and (j–l) batch models ($B = 0$). All simulations are run for 11 Myr. The red line in Figure 3h ($t_{MO} = 1$ Myr and $B = 1.8$) corresponds to the model shown in Figure 2. For batch models, only simulations with Ra_{ref} of 10^7 have been performed. The dotted line marks the end of the crystallization for each case in Figures 3a–3l.

can be recognized in the time series of Nu_{bot} shown in Figure 3. On the one hand, when the overturn takes place only after the whole mantle has solidified, e.g., as in Figures 3a, 3d, and 3g, for $t_{MO} = 0.1$ Myr, Nu_{bot} initially grows rapidly because of the sudden cooling of the deep mantle due to the sinking of cold and shallow cumulates. After reaching the first peak, it decreases since the dense overturned cumulates tend to hinder convection and heat extraction from the CMB. On the other hand, in those cases where an early onset is observed (see, e.g., Figures 3c, 3f, and 3i), the first overturn results in the temporary formation of a stably stratified layer atop the CMB. If Ra_{ref} is sufficiently large, this layer can then be quickly destabilized, leading to a second growth of Nu_{bot} (Figures 3c, 3f, and 3i).

The batch crystallization cases exhibit very different convective regimes, mainly due to their melt fraction-dependent rheology and their purely thermal convection. Despite the lower value of the reference Rayleigh number ($Ra_{ref} = 10^7$), the effective Rayleigh number is actually very large both because of the higher initial temperature (T_{RCMF} instead of T_{sol} used in the fractional cases) and of the additional effect of interstitial melt on the rheology (equation (11)), yielding a maximum reached Rayleigh number of 5.45×10^9.
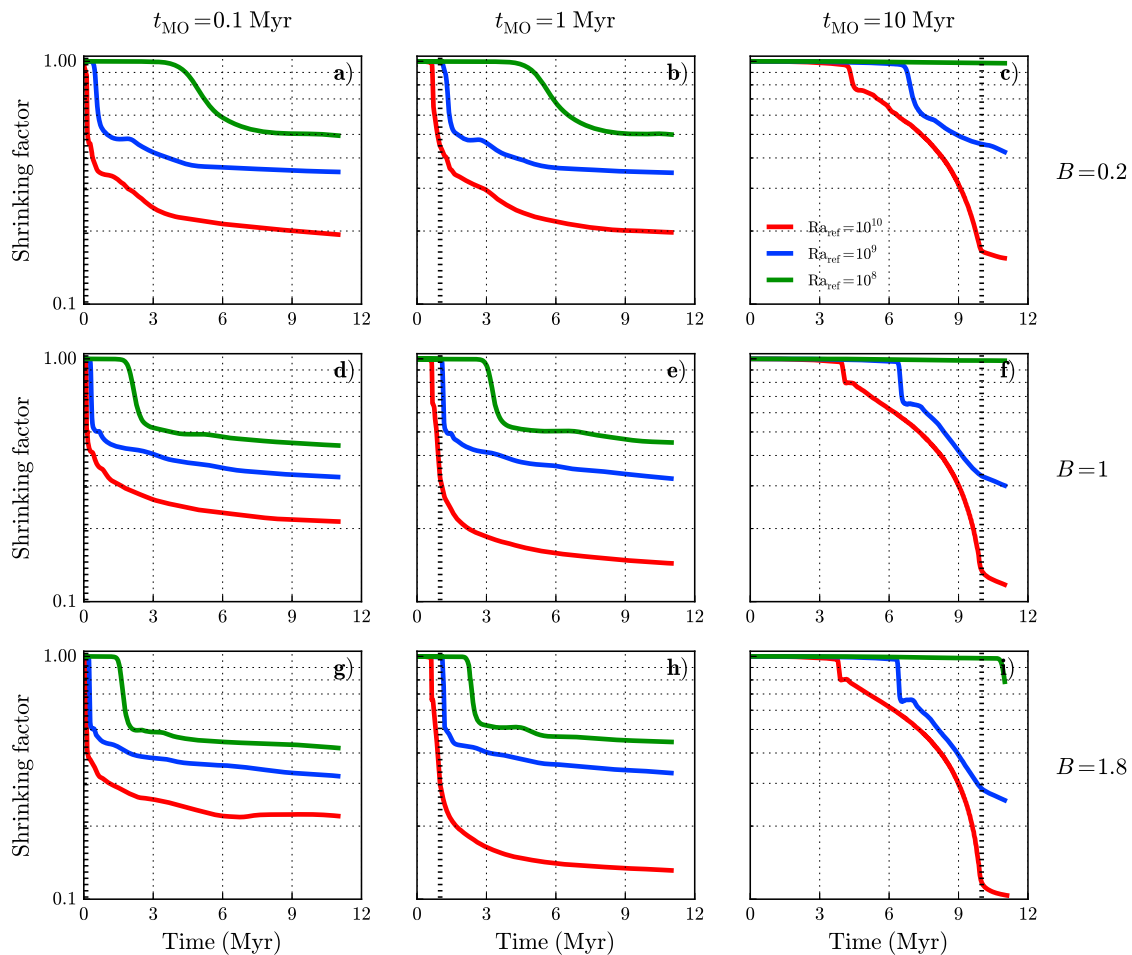
Figure 4. Semilog plots of the time series of the shrinking factor for all combinations of parameters. Similar to Figure 3, the dotted line marks the end of the magma ocean solidification.

While the time for the onset of convection is comparable to that of the fractional crystallization cases with a similar effective Rayleigh number (Figures 3j, 3k, and 3l), the evolution of Nu_{bot} differs considerably. The initial overturn is purely thermal, hence less abrupt, and does not prevent subsequent convection as it is not followed by the formation of a stable compositional gradient. The strong decrease of the viscosity due to its dependence on the melt fraction concentrates the deformation in very thin, rapidly ascending plumes, while cold downwellings, whose viscosity is only controlled by temperature, are slow and diffused (not shown). As a consequence, basal heat is extracted rather inefficiently through these very thin channels, ultimately resulting in much lower values of Nu_{bot}.

3.2. Mantle Mixing

Whether or not solid-state convection starts during the magma ocean phase has a critical influence on the degree of mixing of compositional heterogeneities achieved immediately after solidification, but also over the long-term evolution of the interior of the mantle. Assessing the degree of mantle mixing at the end of magma ocean solidification is important because early-formed compositional heterogeneities can strongly affect the subsequent thermal evolution of the mantle. To measure the degree of mixing of the solid mantle as a function of time, we computed for all simulations the evolution of the shrinking factor as described in section 2.5. Time series for the averaged value of the shrinking factor are displayed in Figure 4.

A late onset of convection leads to a sharp decrease in this quantity. This feature is due to the initial whole-mantle overturn, which causes the slope of the time series to become increasingly steeper as Ra_{ref} and B, and thus the effective Rayleigh number become larger. The subsequent convection causes a further decrease of the shrinking factor toward a quasi-asymptotic value, which also depends on Ra_{ref} and B. In the cases characterized by an early onset of convection (Figures 4c, 4f, and 4i), the initial overturn is still marked by
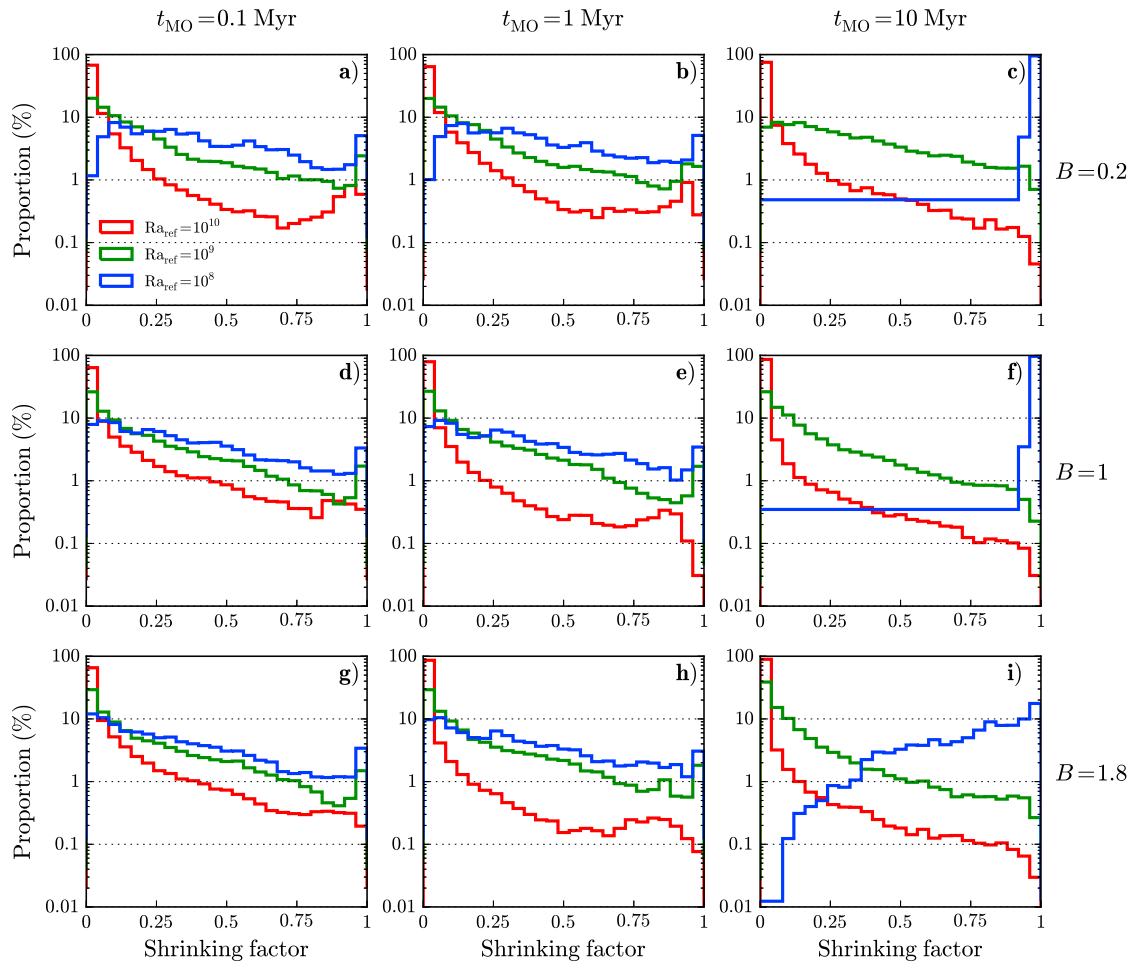
Figure 5. Histograms of the distribution of the shrinking factor after 11 Myr for all simulations. The vertical axis represents (in log scale) the percentage of tracers having a shrinking factor around the value indicated on the horizontal axis.

a sharp decrease of the shrinking factor, whose amplitude is also controlled by the effective Rayleigh number. As in the previous cases, the slope of the time series is steeper for higher Ra_{ref} and B. After the first overturn, the shrinking factor further decreases approximately linearly with time until the end of solidification due to the progressive mixing of the dense, newly crystallized layers. In this phase, mixing accelerates when, after the initial overturn, the first deposited dense layers are progressively reentrained in the flow. The shrinking factor, eventually, evolves as before toward a slowly decreasing value.

Mixing is a typically heterogeneous process in the mantle. For example, the shallowest layers of the mantle are rapidly exposed to the low surface temperature and form a conductive stagnant lid that is too viscous to experience significant deformation. Figure 5 shows the distribution of the shrinking factor across the solid mantle for all simulations after 11 Myr. A homogeneously high shrinking factor close to one indicates that convection has not set in before the end of the 11 Myr (although it starts later, as indicated in section 3.1). The cases for which mixing was mostly efficient have shrinking factors close to 0 (see, e.g., red histograms in Figures 5f and 5i). The presence of a cluster of high shrinking factor values in all simulations is associated with the formation of the stagnant lid. This is mostly evident in the cases presenting a late onset of convection (for instance, all cases with $Ra_{ref} = 10^8$), as previously discussed by *Plesa et al.* [2014]. Nonetheless, a stagnant lid also forms in the cases exhibiting an early onset of convection, and its thickness decreases with increasing B. Indeed, a high value of B destabilizes the upper boundary layer by increasing its compositional density gradient. In general, a high value of Ra_{ref} generates small-scale convective patterns and an increased time dependence of the flow that enhances mantle mixing, causing the shrinking factor to cluster around values close to 0. A low Ra_{ref} leads instead to longer wavelength convection that ultimately results in a large spread of the shrinking factor values. When B is large enough, cases characterized by a late whole-mantle overturn
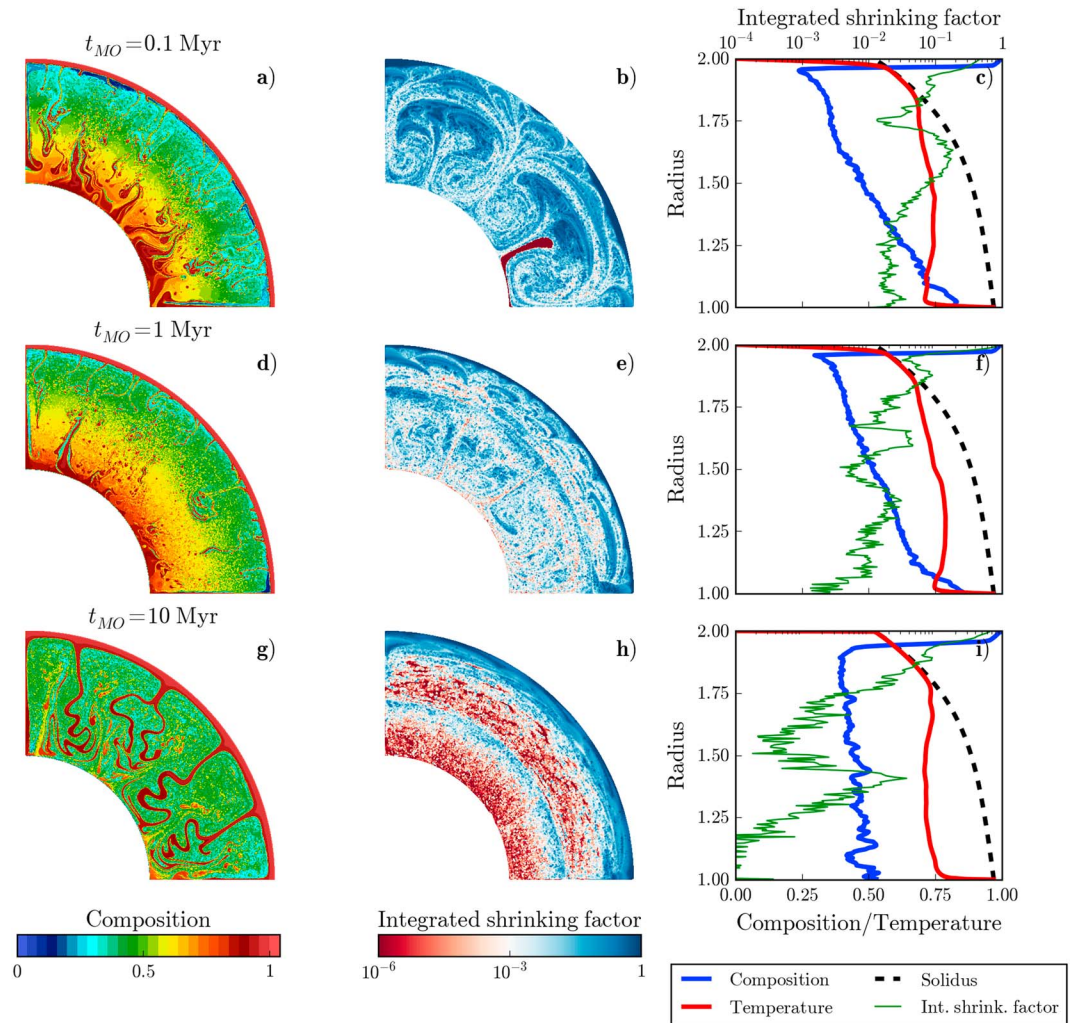
Figure 6. Snapshots of the (a, d, and g) composition field, (d, e, and f) integrated shrinking factor, and (c, f, and i) laterally averaged profiles of composition, temperature, and integrated shrinking factor after 11 Myr for simulations assuming fractional crystallization with $B = 1.8$, $Ra = 10^{10}$, and different solidification times ($t_{MO} = 0.1$ Myr in Figures 6a–6c, $t_{MO} = 1$ Myr in Figures 6d–6f, and $t_{MO} = 10$ Myr in Figures 6g–6i). The integrated shrinking factor is a mapping of the final value of the shrinking factor of each tracer, plotted at the initial position of the tracer.

result in a dense layer at the bottom of the mantle that does not take part in the subsequent mixing, limiting the convection to the upper layers below the stagnant lid, provided that Ra_{ref} is high enough to sustain it. This convecting zone experiences prolonged mixing, while the bottom layer experiences just limited shrinking during the overturn, resulting in a significant spread in the values of the shrinking factor (see red histogram on Figure 5g).

The heterogeneity of solid-state mixing is illustrated in Figure 6, where we compare simulations with different solidification times for the case $B = 1.8$ and $Ra_{ref} = 10^{10}$. The figure shows, after 11 Myr, snapshots of the composition field (Figures 6a, 6d, and 6g), of the integrated shrinking factor (Figures 6b, 6e, and 6h), and laterally averaged profiles (Figures 6c, 6f, and 6i) of temperature (red line), composition (blue line), and integrated shrinking factor (green line). The latter represents the final value of the shrinking factor calculated and mapped according to the initial position of tracers distributed throughout the domain that has, after 11 Myr, experienced a certain level of mixing. A region with a high (respectively, low) value of the integrated shrinking factor indicates thus that the mantle's material initially located in that specific region has undergone a poor (respectively, intense) mixing.

The case with $t_{MO} = 0.1$ Myr (Figures 6a–6c) is characterized by a late onset of convection, with a large-scale overturn taking place underneath a newly formed stagnant lid. This global overturn results in a

compositionally layered structure as shown in Figure 6a and by the blue profile of Figure 6c. The uppermost layers located beneath the stagnant lid sink to the CMB and remain there. These layers thus experience considerably less shrinking than other parts of the mantle that are involved in the subsequent convection. These poorly mixed cumulates originate from the region marked by the two dark blue areas in Figure 6b corresponding to the local maximum of the profile in Figure 6c located at a nondimensional radius between 1.50 and 1.75. Note that after the initial overturn, thermal convection is not immediately suppressed by the stable compositional gradient but continues below the stagnant lid, causing this to thin from its initial thickness of ∼25% of the mantle's depth to its final thickness as seen in Figures 6a and 6c. It is also worth noting the presence of a rather small region characterized by a very low value of the integrated shrinking factor (red spot on Figure 6b). Tracers initially located in this region were first advected in an upwelling plume that turned later into a downwelling, thereby generating significant shrinking over the analyzed time interval.

The second case with $t_{MO} = 1$ Myr (Figures 6e–6f) exhibits an early onset of convection. However, the initial overturn occurs near the end of the crystallization, making it qualitatively similar to the previous case. Yet an early onset promotes mixing (Figure 6d) and, as a consequence, this case is characterized by a generally lower value of the integrated shrinking factor (i.e., more efficient mixing) throughout the mantle (Figure 6f).

The last case with $t_{MO} = 10$ Myr (Figures 6g–6i) presents a very different mixing pattern. Due to the long-lived magma ocean, the first overturn occurs early during solidification and causes a first layer located at midmantle depth to sink to the CMB where it remains unmixed for some time (see blue stripe at midmantle depth in Figure 6h and local maximum of the green profile in Figure 6i), while the initially underlying material is entrained by vigorous thermal convection. By the end of the solidification, the density heterogeneity has been progressively erased by convective mixing (see blue profile on Figure 6i), and even the material that accumulated at the CMB after the first overturn is reentrained in the bulk of the mantle by convection (no dense layer is present atop the CMB on Figure 6g), while the newly crystallized uppermost layers of the stagnant lid are progressively entrained by large downwellings.

4. Discussion

4.1. Early and Late Onset of Convection and Mixing

The influences of the different parameters on the final state of the mantle are not straightforward to define because they are not always monotonic and some are coupled with one another. Figure 7 presents the final value (after 11 Myr) of the average shrinking factor for all simulations covering the entire parameter space investigated. Each diagram is divided in two domains according to the time of onset of convection in the simulations (early or late onset). As expected, the reference Rayleigh number has a clear monotonic influence on the onset of convection and on the degree of mixing [*Samuel et al.*, 2011; *Samuel and Tosi*, 2012]. However, the dependence of the final value of the shrinking factor on the buoyancy ratio B and on the solidification time t_{MO} is more complex. In particular, two opposite effects of t_{MO} can be identified:

1. When convection starts only after complete solidification ("late onset" in Figure 7), its onset occurs earlier for lower values of t_{MO} because the thermal and compositional density contrasts across the mantle become available earlier, i.e., the final value of the effective Rayleigh number is reached sooner. As a consequence, convection has more time to mix the mantle, so that by the end of the simulation time, a higher level of mixing (i.e., a smaller shrinking factor) is achieved, which is further enhanced by increasing the buoyancy ratio.

2. When convection starts before the end of solidification ("early onset" in Figure 7), the mixing of the solid cumulates is more efficient during solidification than after it, because the continuous formation of denser and denser material at the top of the solid cumulates acts as a supplementary source of buoyancy. Mixing during solidification also erases efficiently compositional heterogeneities, avoiding the formation of a stably stratified structure that would hinder subsequent thermal convection. Therefore, in these cases, a better mixing is achieved both for a longer t_{MO} as well as for a higher B.

The influence of t_{MO} is controlled by both Ra_{ref} and B. For low values of Ra_{ref}, the first effect discussed above is dominant because an early onset of convection is less likely, and a higher degree of mixing is achieved for lower t_{MO} (compare the upper rows of the three diagrams in Figure 7). For high values of Ra_{ref}, the second effect becomes dominant and the opposite trend is observed (compare the bottom rows in Figure 7). For intermediate values of Ra_{ref}, the transition from the first to the second effect occurs upon increasing B (compare the middle rows in Figure 7). Note that in case of early onset, although high values of B enhance
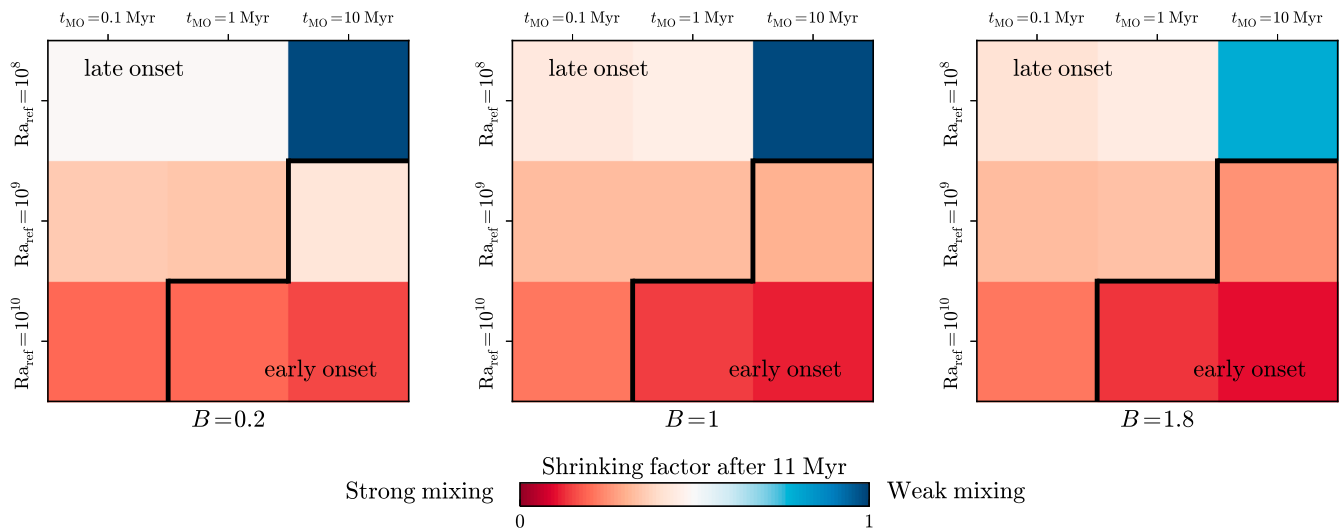
Figure 7. Mean shrinking factor after 11 Myr for all simulations as a function of t_{MO} and Ra_{ref} for the three different values of B. The color scale is linear.

mixing at the end of solidification as shown in Figure 7, they also increase the absolute density contrasts. As a consequence, cases with a high value of B still tend to end up with a stronger stable compositional gradient in the bulk convecting mantle than cases with a low value of B.

4.2. Application to Mars's Mantle
4.2.1. Plausible Parameter Range for Mars

The reference Rayleigh number for the early Martian mantle is poorly constrained, particularly because of the large uncertainties in the mantle rheology. Among the numerous factors that affect the reference viscosity, which enters the Rayleigh number, the water content is particularly critical because of the wide range of possible values it can take [e.g., *Ruedas et al.*, 2013; *Breuer et al.*, 2016]. From the analysis of the SNC meteorites, water concentrations in the mantle source regions have been estimated to range from 55 to 160 ppm for the depleted shergottites and from 120 to 220 ppm for the enriched ones [*Watson et al.*, 1994; *Leshin*, 2000; *McCubbin et al.*, 2012]. If the above ranges were also representative for the solid cumulates that formed during magma ocean solidification, the water concentration of the early Martian mantle may have been even higher than the maximum value assumed here of 100 ppm, for which we have $Ra_{ref} = 10^{10}$. Testing the effects of higher water concentrations, i.e., of higher reference Rayleigh numbers, has proven computationally challenging. Yet increasing Ra_{ref} by lowering the reference viscosity would simply imply an earlier onset of convection and more efficient mantle mixing. For comparison, note that *Elkins-Tanton et al.* [2005a] used $Ra_{ref} = 3 \times 10^9$, albeit in the context of isoviscous simulations.

Also note that we have not considered the effects of stress-dependent, non-Newtonian viscosity. This kind of rheology, which is often mimicked by simply using a Newtonian viscosity of diffusion creep with a reduced activation energy [e.g., *Scheinberg et al.*, 2014], could be relevant for Mars and have an important influence on the onset time of convection and on mantle mixing. In particular, the first overturn is likely to induce large shear stresses that in turn could reduce the viscosity even further. This is an important issue that should be addressed in future studies.

The buoyancy ratio ultimately depends on the amount of iron present in the mantle and on how it is partitioned between the melt and the solid matrix as the mantle solidifies under the assumption that this occurs through fractional crystallization. In a recent review, *Taylor* [2013] suggested an iron oxide content of around 18 wt % for the bulk mantle plus crust reservoir. In the case of a linear compositional gradient (completely iron depleted at the bottom), this abundance would result in a buoyancy ratio 0.86, assuming that iron replaces magnesium oxide (which is in excess compared to iron oxide) in the solid cumulates as crystallization proceeds. The crystallization sequence proposed by *Elkins-Tanton et al.* [2005a] results in a very large B of 3.34. This value was employed by *Plesa et al.* [2014] to simulate a whole-mantle overturn and to show that with such a large buoyancy ratio, post-overturn mantle convection and melting would be strongly inhibited. The values of B that we tested in this study ($B \leq 1.8$) are lower than the value predicted by *Elkins-Tanton et al.* [2005a] but close to the values based on *Taylor* [2013] and a simple linear profile.

In our analysis of the early onset of solid-state convection, the timescale of mantle solidification t_{MO} plays a central role. For this, the initial volatile content of the planet is of fundamental importance as it can determine the emergence of an insulating atmosphere generated upon magma ocean solidification and degassing. Along with water, the CO_2 content of the mantle is also essential because of its greenhouse potential as a gas. *Debaille et al.* [2007] suggest a long-lived Martian magma ocean with a lifetime in excess of 100–200 Myr based on Sm-Nd systematics of shergottites. This timescale, however, is significantly longer than that determined using coupled interior-atmosphere models of mantle solidification. Assuming 0.6 wt % content of CO_2 and no water, *Elkins-Tanton* [2008] found that a 2000 km deep magma ocean on Mars would solidify in less than 3 Myr, while *Lebrun et al.* [2013] obtained solidification times of about 1 Myr assuming 420 ppm H_2O and 140 ppm CO_2. Both estimates are thus in line with our choice of $t_{MO} \leq 10$ Myr.

In summary, despite significant uncertainties in the parameters that govern the early dynamics of solid mantle cumulates, it seems likely that the Martian mantle may have been at least partly mixed by the time the magma ocean solidified, which calls into question the scenario of a whole-mantle overturn that has been often used as a starting condition for several simulations of interior evolution.

4.2.2. Martian Geochemical Reservoirs

The isotopic analysis of the Martian meteorites reveals large variations in lithophile radiogenic isotope systems such as $^{87}Rb-^{86}Sr$, $^{147,146}Sm-^{143,142}Nd$, and $^{176}Lu-^{176}Hf$ and suggests the existence of three to four distinct chemical reservoirs [e.g., *Jagoutz*, 1991; *Foley et al.*, 2005]. The range of crystallization ages determined for these samples, from 4.5 Ga to 160 Ma [*Nakamura et al.*, 1982a, 1982b; *Nyquist et al.*, 2001; *Humayun et al.*, 2013; *Agee et al.*, 2013], indicates that their source reservoirs have been preserved over the entire thermochemical evolution of Mars. To explain such system, the scenario of a global cumulate overturn has been invoked in previous studies because of its ability to create a stable density configuration, which easily allows the isotopic signature of various reservoirs to be preserved until present day [*Elkins-Tanton et al.*, 2005a, 2005b]. However, the predicted compositional density gradient following the crystallization and global overturn of the magma ocean, albeit being able to form and maintain distinct reservoirs over the entire thermochemical evolution of the planet, is too large to allow subsequent thermochemical convection, with the consequence that sampling of the various mantle sources through partial melting is unlikely [*Tosi et al.*, 2013; *Plesa et al.*, 2014]. The crystallization of the liquid magma ocean is a highly dynamical process and, as shown in this study, the onset of solid-state convection well before complete solidification may strongly reduce chemical heterogeneities. In fact, a more suitable scenario would require smaller density gradients to be present at the end of the crystallization phase, so that reservoirs can be sampled by subsequently formed mantle plumes and partial melting. This configuration can be achieved through progressive mixing of the solid cumulate due to an early onset of convection.

It should be noted that *Ogawa and Yanagisawa* [2011] and *Plesa and Breuer* [2014] proposed differentiation due to secondary melting in an initially hot and homogeneous post-magma ocean mantle as an alternative way to generate—and possibly preserve—large-scale compositional heterogeneities. This mechanism, as proposed by the above authors, would apply in the case of a magma ocean undergoing batch crystallization. However, in the case of fractional crystallization, and particularly if the mantle experienced an early onset of convection and hence partial mixing, it is not straightforward to predict to which extent primordial compositional anomalies generated by magma ocean fractionation would affect the subsequent differentiation associated with partial melting of the solidified mantle.

4.3. A More Realistic Evolution of Mantle Solidification

The linear unstable density profile that was used in this and previous works [*Zaranek and Parmentier*, 2004; *Tosi et al.*, 2013; *Elkins-Tanton et al.*, 2005a] is only a crude approximation of the density profile obtained with models of fractional crystallization [e.g., *Elkins-Tanton et al.*, 2003, 2005a]. Its actual shape influences both the onset time of convection, because it affects directly the evolution of the effective Rayleigh number and the degree of mixing achieved at the end of solidification since it determines the local density gradient in the upper boundary layer where newly crystallized material is located. Realistic profiles are typically characterized by a relatively flat gradient in the deep mantle that grows steeper and steeper close to the surface because of the evolution of the iron partitioning coefficient with pressure. Since we have demonstrated that the buoyancy ratio has only a small influence on the onset of convection (Figure 3), for a given Ra_{ref} and t_{MO}, the use of a more realistic crystallization sequence would only result in a slightly delayed onset time.

A constant cooling rate of the magma ocean is also only a first-order approximation of the solidification evolution. A volumetrically constant solidification rate would result in a slower solidification of the shallower layers with respect to the deeper ones. Furthermore, the heat flow through a turbulent liquid magma ocean scales with the Rayleigh number of the magma ocean ($Ra_{MO} \sim 10^{20} - 10^{30}$) to an exponent varying between 1/3 and 2/7 [*Solomatov*, 2007]. Thus, heat is less efficiently extracted as the magma ocean becomes shallower, i.e., as its Rayleigh number decreases. If no atmosphere is formed during the solidification, the radiative heat loss at the surface of the planet decreases with the surface temperature of the planet to the fourth power, while if a blanketing atmosphere is outgassed, the heat escape may be considerably slowed down [*Lebrun et al.*, 2013]. The evolution of the different heat fluxes all act in favor of a decrease of the solidification rate with time, i.e., a slower solidification of the shallower layers. A more realistic solidification evolution is thus likely characterized by a lower mantle that solidifies rapidly, possibly via batch crystallization, and an upper mantle that solidifies much more slowly, probably via fractional crystallization.

The time evolution of the solidification front would also be influenced by the release of latent heat during crystallization. Since the crystallization time is imposed and not modeled self-consistently, latent heat effects are implicitly incorporated in its parameterization and, in any case, they are not relevant for the fractional crystallization cases where only subsolidus temperatures are considered. For the batch crystallization cases, instead, latent heat effects would have to be considered in the mush domain. For a specific case with $t_{MO} = 10$ Myr, we carried out an additional simulation including latent heat, which we took into account by adding the term $-L\partial\phi/\partial t$ to the right-hand side of the thermal energy equation (6). The addition of latent heat acts as a local heat source upon solidification, which tends to equalize temperature differences and, in turn, to slightly retard the growth of the imposed initial perturbation. As a consequence, we observed an onset of convection delayed by about 10% with respect to the corresponding case where latent heat was neglected.

4.4. Application to Other Terrestrial Bodies
The terrestrial bodies of the inner solar system including (and in particular) the Moon are thought to have experienced magma ocean episodes [*Elkins-Tanton*, 2012]. However, these bodies have largely different properties, which likely resulted in different solidification scenarios. Below we discuss how the major terrestrial bodies would fit in the parameter space that we explored.

The reference Rayleigh number is largely controlled by the size of the body, while the buoyancy ratio, indicative of its mantle's iron content, might increase with distance from the Sun as a result of the accretion history [*Taylor*, 2013]. Assessing the initial volatile content is extremely speculative; therefore, the lifetime of the magma ocean is probably the least constrained parameter.

4.4.1. Earth
The Earth's mantle is 1.7 times as deep as Mars's, which increases the reference Rayleigh number by a factor 5. Although it formed from a volatile-depleted zone of the protoplanetary disk [*Carlson et al.*, 2014], and the mechanisms involved in the delivery of volatile on Earth are not clearly identified, it is likely that Earth's water content was delivered during planetary formation [*Morbidelli et al.*, 2012], so that it was already available by the time of the magma ocean solidification. The Earth can thus have developed a thick blanketing atmosphere, able to sustain a long-lived magma ocean [e.g., *Abe*, 1993; *Zahnle et al.*, 2007; *Lebrun et al.*, 2013]. According to our results, a late magma ocean on Earth is likely to have experienced solid cumulate mixing during its crystallization, resulting in a roughly homogeneous mantle structure, even though the pressure dependence of the rheology, more relevant for the Earth than for Mars because of the higher pressure range, may have caused a less efficient mixing of the lower mantle. This scenario still has to be compared with present-day possible traces of a past magma ocean, in particular, with the presence of large low-shear-velocity provinces at the core-mantle boundary [e.g., *Garnero et al.*, 2016] that could be the product of the fractional crystallization of a long-lived basal magma ocean [*Labrosse et al.*, 2007].

4.4.2. Venus
Venus and Earth are similar in many respects; in particular, they have nearly the same size and, possibly, also the same bulk composition [*Fegley*, 2005], although their present-day surface conditions are very different. The evolution of a putative magma ocean will clearly depend on the early surface conditions on Venus, which are essentially unconstrained. Nevertheless, it should be noted that, depending on its initial water content, Venus could have sustained a magma ocean for more than 100 Myr [*Hamano et al.*, 2013] (defined in this paper as the time until which the surface temperature reaches the solidus). This, together with a high Rayleigh

number comparable with that of the Earth, may have resulted in highly efficient mixing during magma ocean solidification and hence in a well homogenized mantle already at the beginning of its evolution.

4.4.3. Moon

In general, based on our results on the onset of convection and mixing during magma ocean solidification, the early lunar mantle is expected to be less homogeneous compared to the mantles of Mars, Venus and Earth, essentially because its effective Rayleigh number is smaller. Furthermore, the low surface gravity on the Moon would likely prevent a thick outgassed atmosphere to be retained for a long time. The presence of anorthositic material over the Moon's surface suggests the formation of a flotation crust resulting from the crystallization of plagioclase minerals toward the end of magma ocean solidification [*Snyder et al.*, 1992]. Although such a crust may have acted to slow down solidification, plagioclase flotation is expected to occur late during crystallization, when about 70 to 85% of the lunar magma ocean has solidified. At this stage, most of the mantle has already crystallized without experiencing substantial solid-state mixing. It has been proposed that the Procellarum KREEP Terrane on the surface of the Moon, an anomalous region highly enriched in incompatible elements, may reflect the sampling of an ilmenite-rich reservoir in the lunar interior. Initially located near the surface during the crystallization of the lunar magma ocean, this ilmenite-rich reservoir may have sunken to the CMB as a consequence of a mantle overturn. Later, its sampling by a degree 1 convection pattern may have produced the signature of the PKT region on the lunar surface [e.g., *Zhong et al.*, 2000; *Stegman et al.*, 2003; *Zhang et al.*, 2013]. This above scenario is compatible with our results, according to which negligible mixing likely took place during the solidification of the lunar magma ocean and a global overturn may have taken place at the end of solidification.

4.4.4. Mercury

With a mantle thickness of only ∼400 km [*Hauck et al.*, 2013], Mercury has the thinnest silicate shell among the terrestrial planets, resulting in a significantly lower Rayleigh number. The relatively high surface abundance of sulfur [*Evans et al.*, 2012], along with the evidence of pyroclastic volcanism [*Thomas et al.*, 2014] indicate that Mercury may be relatively rich in volatiles. However, its proximity to the Sun suggests that it should have formed in a hot region of the protoplanetary disk from volatile-depleted materials [*Fegley and Cameron*, 1987], which makes unlikely the outgassing of a significant blanketing atmosphere able to survive escape processes. A rapid cooling of Mercury's magma ocean may have prevented crystal-melt separation during crystallization, thus leading to a rather homogeneous mantle. Nevertheless, spectroscopic measurements of Mercury's surface materials performed during the MESSENGER mission have revealed the existence of compositionally distinct signatures [*Weider et al.*, 2015]. As for the Moon, fractional crystallization of a magma ocean characterized by a late stage involving the flotation of buoyant crystals—graphite in the case of Mercury [*Vander Kaaden and McCubbin*, 2015]—and accompanied by a whole-mantle overturn seems then to be a viable scenario [*Brown and Elkins-Tanton*, 2009; *Charlier et al.*, 2013].

5. Conclusions

The solidification of a magma ocean during the early stages of the evolution of terrestrial bodies is often assumed to be a rapid process, occurring within thousands of years [e.g., *Monteux et al.*, 2016] because of the very efficient radiative cooling of the hot surface in contact with cold space. In case of a rapid solidification, batch crystallization, which results in a homogeneous mantle, or fractional crystallization followed by a global overturn, which results in a stably stratified mantle, can take place. Nevertheless, outgassing of a blanketing atmosphere can retard heat escape and sustain a magma ocean for a few million years [*Elkins-Tanton*, 2008; *Lebrun et al.*, 2013] up to hundreds of million years for bodies, like Venus, that experience a strong insolation [*Hamano et al.*, 2013]. We showed that because of the low viscosity of the hot solid cumulates, potentially further decreased by the presence of water and residual melt, a solidification time of ∼1 Myr is sufficient for solid-state convection to begin during the crystallization of the magma ocean and to start mixing the unstable compositional density gradient resulting from iron partitioning during fractional crystallization. For the longest magma ocean's lifetime tested (10 Myr) and for a sufficiently high-reference Rayleigh number ($Ra_{ref} \gtrsim 10^9$), a high level of mixing of the solid cumulates can be achieved by the end of the solidification. In this situation, compositional heterogeneities are at least partly erased during the early evolution, with the consequence that the traditional scenario of a whole-mantle overturn becomes unlikely.

Our results thus suggest that the initial compositional structure of the mantle can be the result of a number of complex and intertwined processes: chemistry of magma ocean crystallization, volatile outgassing and

formation of a blanketing atmosphere, and solid-state mantle convection, a process that has not been taken into consideration so far. Future efforts aimed at combining these approaches in a self-consistent way will help to better constrain the initial conditions of the interior in view of its long-term thermochemical evolution.

References

Abe, Y. (1993), Thermal and chemical evolution of the terrestrial magma ocean, *Phys. Earth Planet. Inter.*, *100*, 27–39.

Abe, Y., and T. Matsui (1985), The formation of an impact-generated H_2O atmosphere and its implications for the thermal history of the Earth, *J. Geophys. Res.*, *90*, 545–559.

Agee, C. B., et al. (2013), Unique meteorite from early Amazonian Mars: Water-rich basaltic breccia Northwest Africa 7034, *Science*, *339*, 780–785, doi:10.1126/science.1228858.

Andrault, D., N. Bolfan-Casanova, G. Lo Nigro, M. A. Bouhifd, G. Garbarino, and M. Mezouar (2011), Solidus and liquidus profiles of chondritic mantle: Implication for melting of the Earth across its history, *Earth Planet. Sci. Lett.*, *304*(1–2), 251–259, doi:10.1016/j.epsl.2011.02.006.

Boukaré, C.-E., Y. Ricard, and G. Fiquet (2015), Thermodynamics of the MgO-FeO-SiO₂ system up to 140 GPa: Application to the crystallization of Earth's magma ocean, *J. Geophys. Res. Planets*, *120*, 6085–6101, doi:10.1002/2015JB011929.

Breuer, D., A.-C. Plesa, N. Tosi, and M. Grott (2016), Water in the Martian interior — The geodynamical perspective, *Meteor. Planet. Sci.*, *51*(11), 1959–1992.

Brown, S. M., and L. T. Elkins-Tanton (2009), Compositions of Mercury's earliest crust from magma ocean models, *Earth Planet. Sci. Lett.*, *286*, 446–455.

Carlson, R. W., et al. (2014), How did early Earth become our modern world?, *Annu. Rev. Earth Planet. Sci.*, *42*, 151–178, doi:10.1146/annurev-earth-060313-055016.

Charlier, B., T. L. Grove, and M. T. Zuber (2013), Phase equilibria of ultramafic compositions on Mercury and the origin of the compositional dichotomy, *Earth Planet. Sci. Lett.*, *363*, 50–60, doi:10.1016/j.epsl.2012.12.021.

Costa, A., L. Caricchi, and N. Bagsdassarov (2009), A model for the rheology of a particle-bearing suspensions and partially molten rocks, *Geochem. Geophys. Geosyst.*, *10*, Q03010, doi:10.1029/2008GC002138.

de Vries, J., A. van den Berg, and W. van Westrenen (2010), Formation and evolution of a lunar core from ilmenite-rich magma ocean cumulates, *Earth Planet. Sci. Lett.*, *292*(1), 139–147.

Debaille, V., A. Brandon, Q. Yin, and B. Jacobsen (2007), Coupled ¹⁴²Nd-¹⁴³Nd evidence for a protracted magma ocean in Mars, *Nature*, *450*(7169), 525–528.

Debaille, V., A. Brandon, C. O'Neill, Q. Yin, and B. Jacobsen (2009), Early Martian mantle overturn inferred from isotopic composition of nakhlite meteorites, *Nat. Geosci.*, *2*(8), 548–552.

Elkins-Tanton, L. (2008), Linked magma ocean solidification and atmospheric growth for Earth and Mars, *Earth Planet. Sci. Lett.*, *271*, 181–191.

Elkins-Tanton, L. (2012), Magma oceans in the inner solar system, *Ann. Rev. Earth Planet. Sci.*, *40*, 113–139.

Elkins-Tanton, L., E. Parmentier, and P. Hess (2003), Magma ocean fractional crystallization and cumulate overturn in terrestrial planets: Implications for Mars, *Meteor. Planet. Sci.*, *38*(12), 1753–1771.

Elkins-Tanton, L. T., S. Zaranek, E. Parmentier, and P. Hess (2005a), Early magnetic field and magmatic activity on Mars from magma ocean cumulate overturn, *Earth Planet. Sci. Lett.*, *236*, 1–12.

Elkins-Tanton, L. T., P. C. Hess, and E. M. Parmentier (2005b), Possible formation of ancient crust on Mars through magma ocean processes, *J. Geophys. Res.*, *110*, E12S01, doi:10.1029/2005JE002480.

Evans, L. G., et al. (2012), Major-element abundances on the surface of Mercury: Results from the MESSENGER Gamma-Ray Spectrometer, *J. Geophys. Res.*, *117*, E00L07, doi:10.1029/2012JE004178.

Farnetani, C., and H. Samuel (2003), Lagrangian structures and stirring in the Earth's mantle, *Earth Planet. Sci. Lett.*, *206*(3), 335–348.

Fegley, B. (2005), Venus, in *Treatise on Geochemistry*, edited by A. Davis, H. Holland, and K. Turekian, pp. 487–507, Elsevier, Amsterdam.

Fegley, B., and A. W. Cameron (1987), A vaporization model for iron/silicate fractionation in the Mercury protoplanet, *Earth Planet. Sci. Lett.*, *82*(3–4), 207–222, doi:10.1016/0012–821X(87)90196–8.

Fiquet, G., A. Auzende, J. Siebert, A. Corgne, H. Bureau, H. Ozawa, and G. Garbarino (2010), Melting of peridotite to 140 gigapascals, *Science*, *329*(5998), 1516–1518, doi:10.1126/science.1192448.

Foley, B. J., D. Bercovici, and L. T. Elkins-Tanton (2014), Initiation of plate tectonics from post-magma ocean thermochemical convection, *J. Geophys. Res. Solid Earth*, *119*, 8538–8561, doi:10.1002/2014JB011121.

Foley, C. N., M. Wadhwa, L. Borg, P. Janney, R. Hines, and T. Grove (2005), The early differentiation history of Mars from ¹⁸²W-¹⁴²Nd isotope systematics in the SNC meteorites, *Geochim. Cosmochim. Acta*, *69*, 4557–4571, doi:10.1016/j.gca.2005.05.009.

Garnero, E. J., A. K. McNamara, and S.-H. Shim (2016), Continent-sized anomalous zones with low seismic velocity at the base of Earth's mantle, *Nat. Geosci.*, *9*, 481–489, doi:10.1038/ngeo2733.

Grott, M., and D. Breuer (2010), On the spatial variability of the Martian elastic lithosphere thickness: Evidence for mantle plumes?, *J. Geophys. Res.*, *115*, E03005, doi:10.1029/2009JE003456.

Gurnis, M. (1986), Stirring and mixing in the mantle by plate-scale flow — Large persistent blobs and long tendrils coexist, *Geophys. Res. Lett.*, *13*(13), 1474–1477.

Hamano, K., Y. Abe, and H. Genda (2013), Emergence of two types of terrestrial planets, *Nature*, *497*, 607–610, doi:10.1038/nature12163.

Hansen, U., and D. Yuen (1995), Formation of layered structures in double-diffusive convection as applied to the geosciences, in *Double Diffusive Convection*, vol. 94, edited by U. Hansen and D. Yuen, pp. 135–150, AGU, Washington, D. C.

Hauck, S., et al. (2013), The curious case of Mercury's internal structure, *J. Geophys. Res. Planets*, *118*, 1204–1220, doi:10.1002/jgre.20091.

Herzberg, C., P. Raterron, and J. Zhang (2000), New experimental observations on the anhydrous solidus for peridotite KLB-1, *Geochem. Geophys. Geosyst.*, *1*, 1051, doi:10.1029/2000GC000089.

Hirth, G., and D. Kohlstedt (2003), Rheology of the upper mantle and the mantle wedge: A view from the experimentalists, in *Inside the Subduction Factory Geophys. Monogr. Ser.*, vol. 138, edited by J. Eiler, pp. 83–105, AGU, Washington, D. C., doi:10.1029/GM138.

Humayun, M., A. Nemchin, B. Zanda, R. H. Hewins, M. Grange, A. Kennedy, J.-P. Lorand, C. Göpel, C. Fieni, S. Pont, and D. Deldicque (2013), Origin and age of the earliest Martian crust from meteorite NWA7533, *Nature*, *503*, 513–516.

Hüttig, C., and K. Stemmer (2013), Finite volume discretization for dynamic viscosities on Voronoi grids, *Phys. Earth Planet. Inter.*, *171*, 137–146, doi:10.1016/j.pepi.2008.07.007.

Hüttig, C., N. Tosi, and W. Moore (2013), An improved formulation of the incompressible Navier-Stokes equations with variable viscosity, *Phys. Earth Planet. Inter.*, *220*, 11–18, doi:10.1016/j.pepi.2013.04.002.

Jagoutz, E. (1991), Chronology of SNC meteorites, *Space Sci. Rev.*, *56*(1), 13–22, doi:10.1007/BF00178386.

Karki, B. B., and L. P. Stixrude (2010), Viscosity of MgSiO₃ liquid at Earth's mantle conditions: Implications for an early magma ocean, *Science*, *328*(5979), 740–742, doi:10.1126/science.1188327.

Korenaga, J., and T. H. Jordan (2003), Physics of multiscale convection in Earth's mantle: Onset of sublithospheric convection, *J. Geophys. Res.*, *108*(B7), doi:10.1029/2002JB001760.

Labrosse, S., J. Hernlund, and N. Coltice (2007), A crystallizing dense magma ocean at the base of the Earth's mantle, *Nature*, *450*(7171), 866–869.

Lebrun, T., H. Massol, E., A. Davaille, E. Marcq, P. Sarda, F. Leblanc, and G. Brandeis (2013), Thermal evolution of an early magma ocean in interaction with the atmosphere, *J. Geophys. Res. Planets*, *118*, 1155–1176, doi:10.1002/jgre.20068.

Leshin, L. A. (2000), Insights into Martian water reservoirs from analyses of Martian meteorite QUE94201, *Geophys. Res. Lett.*, *27*(14), 2017–2020.

Li, Q., and W. S. Kiefer (2007), Mantle convection and magma production on present day Mars: Effects of temperature-dependent rheology, *Geophys. Res. Lett.*, *34*, L16203, doi:10.1029/2007GL030544.

McCubbin, F. M., E. H. Hauri, S. M. Elardo, K. E. Vander Kaaden, J. Wang, and C. K. Shearer (2012), Hydrous melting of the Martian mantle produced both depleted and enriched shergottites, *Geology*, *40*(8), 683–686.

Monteux, J., D. Andrault, and H. Samuel (2016), On the cooling of a deep terrestrial magma ocean, *Earth Planet. Sci. Lett.*, *448*, 140–149, doi:10.1016/j.epsl.2016.05.010.

Morbidelli, A., J. I. Lunine, D. P. O'Brien, S. N. Raymond, and K. J. Walsh (2012), Building terrestrial planets, *Ann. Rev. Earth Planet. Sci.*, *40*, 251–275, doi:10.1146/annurev-earth-042711-105319.

Nakamura, N., D. M. Unruh, M. Tatsumoto, and R. Hutchinson (1982a), Origin and evolution of the Nakhla meteorite inferred from Sm-Nd and U-Pb systematics, and REE, Ba, Sr, Rb, and K abundances, *Geochim. Cosmochim. Acta*, *46*, 1555–1573.

Nakamura, N., H. Kogi, and H. Kagami (1982b), Rb-Sr isotopic and REE abundances in the Chassigny meteorite, *Meteoritics*, *17*, 257–258.

Nyquist, L. E., D. D. Bogard, C.-Y. Shih, A. Greshake, D. Stöffler, and O. Eugster (2001), Ages and geologic histories of Martian meteorites, *Chronol. Evol. Mars*, *96*, 105–164.

Ogawa, M., and T. Yanagisawa (2011), Numerical models of Martian evolution induced by magmatism and solid-state convection beneath stagnant lithosphere, *J. Geophys. Res.*, *116*, E08008, doi:10.1029/2010JE003777.

Olson, P., D. A. Yuen, and D. Balsinger (1984), Mixing of passive heterogeneities by mantle convection, *J. Geophys. Res.*, *89*, 425–436.

O'Neill, C., A. Lenardic, L. Moresi, T. Torsvik, and C.-T. Lee (2007), Melt propagation and volcanism in mantle convection simulations, with applications for Martian volcanic and atmospheric evolution, *J. Geophys. Res.*, *112*, E07003, doi:10.1029/2006JE002799.

O'Neill, C., V. Debaille, and W. Griffin (2013), Deep Earth recycling in the Hadean and constraints on surface tectonics, *Am. J. Sci.*, *313*, 912–932.

O'Neill, C., A. Lenardic, M. Weller, L. Moresi, S. Quenette, and S. Zhang (2016), A window for plate tectonics in terrestrial planet evolution?, *Phys. Earth Planet. Inter.*, *255*, 80–92.

Ottino, J. M. (1989), *The Kinematics of Mixing: Stretching, Chaos and Transport*, 363 pp., Cambridge Univ. Press, Cambridge, U. K.

Plesa, A.-C., N. Tosi, and D. Breuer (2014), Can a fractionally crystallized magma ocean explain the thermo-chemical evolution of Mars?, *Earth Planet. Sci. Lett.*, *403*, 225–235, doi:10.1016/j.epsl.2014.06.034.

Plesa, A.-C., N. Tosi, and C. Hüttig (2012), Thermochemical convection in planetary mantles: Advection methods and magma ocean overturn simulations, in *Integrated Information and Computing Systems for Natural, Spatial, and Social Sciences*, edited by C.-P. Rueckemann, pp. 302–323, IGI Global, Hershey, doi:10.4018/978-1-4666-2190-9.ch015.

Plesa, A.-C., and D. Breuer (2014), Partial melting in one-plate planets: Implications for thermo-chemical and atmospheric evolution, *Planet. Space Sci.*, *98*, 50–65, doi:10.1016/j.pss.2013.10.007.

Reese, C., and V. Solomatov (2006), Fluid dynamics of local Martian magma oceans, *Icarus*, *184*(1), 102–120, doi:10.1016/j.icarus.2006.04.008.

Roberts, J. H., and S. Zhong (2006), Degree-1 convection in the Martian mantle and the origin of the hemispheric dichotomy, *J. Geophys. Res.*, *111*, E06013, doi:10.1029/2005JE002668.

Rubie, D. C., F. Nimmo, and H. J. Melosh (2015), Formation of the Earth's core, in *Treatise on Geophysics*, vol. 9, 2nd ed., chap. 3, edited by G. Schubert, pp. 43–79, Elsevier, Amsterdam.

Ruedas, T., P. J. Tackley, and S. C. Solomon (2013), Thermal and compositional evolution of the Martian mantle: Effects of water, *Phys. Earth Planet. Inter.*, *20*, 50–72.

Saar, M. O., M. Manga, K. Cashman, and S. Fremouw (2001), Numerical models of the onset of yield strength in crystal-melt suspensions, *Earth Planet. Sci. Lett.*, *187*(3), 367–379, doi:10.1016/S0012-821X(01)00289-8.

Samuel, H., and S. D. King (2014), Mixing at mid-ocean ridges controlled by small-scale convection and plate motion, *Nat. Geosci.*, *7*(8), 602–605, doi:10.1038/ngeo2208.

Samuel, H., and N. Tosi (2012), The influence of post-perovskite strength on the Earth's mantle thermal and chemical evolution, *Earth Planet. Sci. Lett.*, *323*, 50–59, doi:10.1016/j.epsl.2012.01.024.

Samuel, H., V. Aleksandrov, and B. Deo (2011), The effect of continents on mantle convective stirring, *Geophys. Res. Lett.*, *38*, L04307, doi:10.1029/2010GL046056.

Scheinberg, A., L. T. Elkins-Tanton, and S. J. Zhong (2014), Timescale and morphology of Martian mantle overturn immediately following magma ocean solidification, *J. Geophys. Res. Planets*, *119*, 454–467, doi:10.1002/2013JE004496.

Schubert, G., D. L. Turcotte, and P. Olson (2001), *Mantle Convection in the Earth and Planets*, 940 pp., Cambridge Univ. Press, Cambridge, U. K.

Scott, T., and D. Kohlstedt (2006), The effect of large melt fraction on the deformation behavior of peridotite, *Earth Planet. Sci. Lett.*, *246*(3), 177–187, doi:10.1016/j.epsl.2006.04.027.

Sekhar, P., and S. D. King (2014), 3D spherical models of Martian mantle convection constrained by melting history, *Earth Planet. Sci. Lett.*, *388*, 27–37, doi:10.1016/j.epsl.2013.11.047.

Snyder, G. A., L. A. Taylor, and C. R. Neal (1992), A chemical model for generating the sources of mare basalts: Combined equilibrium and fractional crystallization of the lunar magmasphere, *Geochim. Cosmochim. Acta*, *56*, 3809–3823.

Solomatov, V. (2000), Fluid dynamics of a terrestrial magma ocean, in *Origin of the Earth and Moon*, edited by R. Canup and K. Righter, pp. 323–338, The Univ. of Arizona Press, Tucson, Ariz.

Solomatov, V. (2007), Magma oceans and primordial mantle differentiation, in *Treatise on Geophysics*, vol. 9, edited by D. Stevenson, pp. 91–119, Elsevier, Amsterdam.

Stegman, D. R., M. Jellinek, S. A. Zatman, J. R. Baumgardner, and M. A. Richards (2003), An early lunar core dynamo driven by thermochemical mantle convection, *Nature*, *421*(6919), 143–146.

Stevenson, D., T. Spohn, and G. Schubert (1983), Magnetism and thermal evolution of the terrestrial planets, *Icarus*, *54*, 466–489.

Stixrude, L., N. de Koker, N. Sun, M. Mookherjee, and B. Karki (2009), Thermodynamics of silicate liquids in the deep Earth, *Earth Planet. Sci. Lett.*, *278*, 226–232, doi:10.1016/j.epsl.2008.12.006.

Taylor, G. J. (2013), The bulk composition of Mars, *Chemie der Erde*, *73*, 401–420.

Thomas, R. J., D. A. Rothery, S. J. Conway, and M. Anand (2014), Long-lived explosive volcanism on Mercury, *Geophys. Res. Lett.*, *41*, 6084–6092, doi:10.1002/2014GL061224.

Tosi, N., A.-C. Plesa, and D. Breuer (2013), Overturn and evolution of a crystallized magma ocean: A numerical parameter study for Mars, *J. Geophys. Res. Planets*, *118*, 1512–1528, doi:10.1002/jgre.20109.

Valley, J. W., et al. (2005), 4.4 bilion years of crustal maturation: Oxygen isotope ratios of magmatic zircon, *Contrib. Mineral. Petrol.*, *150*, 561–580, doi:10.1007/s00410-005-025-8.

Vander Kaaden, K. E., and F. M. McCubbin (2015), Exotic crust formation on Mercury: Consequences of a shallow, FeO-poor mantle, *J. Geophys. Res. Planets*, *120*, 195–209, doi:10.1002/2014JE004733.

Watson, L. L., I. D. Hutcheon, S. Epstein, and E. M. Stolper (1994), Water on Mars: Clues from deuterium/hydrogen and water contents of hydrous phases in SNC meteorites, *Science*, *265*(5168), 86–90.

Weider, S. Z., et al. (2015), Evidence for geochemical terranes on Mercury: Global mapping of major elements with MESSENGER's X-Ray Spectrometer, *Earth Planet. Sci. Lett.*, *416*, 109–120.

Zahnle, K., J. Kasting, and J. Pollack (1988), Evolution of a steam atmosphere during Earth's accretion, *Icarus*, *74*, 62–97.

Zahnle, K., N. Arndt, C. Cockell, A. Halliday, E. Nisbet, F. Selsis, and N. H. Sleep (2007), Emergence of a habitable planet, *Space Sci. Rev.*, *129*, 35–78, doi:10.1007/s11214-007-9225-z.

Zaranek, S., and E. Parmentier (2004), Convective cooling of an initially stably stratified fluid with temperature-dependent viscosity: Implications for the role of solid-state convection in planetary evolution, *J. Geophys. Res.*, *109*, B03409, doi:10.1029/2003JB002462.

Zhang, J., and C. Herzberg (1994), Melting experiments on anhydrous peridotite KLB-1 from 5.0 to 22.5 GPA, *J. Geophys. Res.*, *99*(B9), 17,729–17,742.

Zhang, N., E. M. Parmentier, and Y. Liang (2013), A 3-D numerical study of the thermal evolution of the Moon after cumulate mantle overturn: The importance of rheology and core solidification, *J. Geophys. Res. Planets*, *118*, 1789–1804, doi:10.1002/jgre.20121.

Zhong, S., E. Parmentier, and M. Zuber (2000), A dynamic origin for the global asymmetry of lunar mare basalts, *Earth Planet. Sci. Lett.*, *177*(3), 131–140.